Westinghouse Non-Proprietary Class 3

WCAP-16081-NP

May 2003

10x10 SVEA Fuel Critical Power Experiments and CPR Correlation: SVEA-96 Optima2

Westinghouse

LEGAL NOTICE

This report was prepared as an account of work performed by Westinghouse Electric Company LLC. Neither Westinghouse Electric Company LLC, nor any person acting on its behalf:

A. Makes any warranty or representation, express or implied including the warranties of fitness for a particular purpose or merchantability, with respect to the accuracy, completeness, or usefulness of the information contained in this report, or that the use of any information, apparatus, method, or process disclosed in this report may not infringe privately owned rights; or

B. Assumes any liabilities with respect to the use of, or for damages resulting from the use of, any information, apparatus, method, or process disclosed in this report.

WCAP-16081-NP

10x10 SVEA Fuel Critical Power Experiments and CPR Correlation: SVEA-96 Optima 2

May 2003

Westinghouse Electric Company LLC
2000 Dayhill Road
Windsor, CT 06095-0500

COPYRIGHT NOTICE

This report has been prepared by Westinghouse Electric Company LLC and bears a Westinghouse Electric Company copyright notice. Information in this report is the property of and contains copyright material owned by Westinghouse Electric Company LLC and /or its subcontractors and suppliers. It is transmitted to you in confidence and trust, and you agree to treat this document and the material contained therein in strict accordance with the terms and conditions of the agreement under which it was provided to you.

As a participating member of this task, you are permitted to make the number of copies of the information contained in this report that are necessary for your internal use in connection with your implementation of the report results for your plant(s) in your normal conduct of business. Should implementation of this report involve a third party, you are permitted to make the number of copies of the information contained in this report that are necessary for the third party's use in supporting your implementation at your plant(s) in your normal conduct of business if you have received the prior, written consent of Westinghouse Electric Company LLC to transmit this information to a third party or parties. All copies made by you must include the copyright notice in all instances and the proprietary notice if the original was identified as proprietary.

The NRC is permitted to make the number of copies beyond those necessary for its internal use that are necessary in order to have one copy available for public viewing in the appropriate docket files in the NRC public document room in Washington, DC if the number of copies submitted is insufficient for this purpose, subject to the applicable federal regulations regarding restrictions on public disclosure to the extent such information has been identified as proprietary. Copies made by the NRC must include the copyright notice in all instances and the proprietary notice if the original was identified as proprietary.

TABLE OF CONTENTS

1 SUMMARY 1-1

2 INTRODUCTION 2-1

3 TEST FACILITY 3-1
3.1 DESCRIPTION 3-1
3.2 TEST SECTION 3-1
3.3 HEATER RODS 3-2
3.4 POWER SUPPLY AND CONTROL 3-4
3.5 INSTRUMENTATION 3-4
3.6 DATA ACQUISITION SYSTEM 3-5
3.7 CRITICAL POWER TESTING PROCEDURE 3-5

4 TEST PROGRAM 4-1
4.1 RANGE OF TEST PARAMETERS 4-1
4.2 JUSTIFICATION FOR RANGE OF TEST PARAMETERS 4-2
4.2.1 Mass Flux 4-2
4.2.2 System Pressure 4-2
4.2.3 Inlet Subcooling 4-2
4.2.4 Axial Power Distribution 4-3
4.2.5 Local Power Distribution 4-3
4.2.6 Combinations of Parameters 4-4
4.2.7 Summary 4-4
4.3 DATA VALIDATION CRITERIA AND PROCEDURES 4-4
4.4 DATA TRENDS 4-5

5 CRITICAL POWER CORRELATION 5-1
5.1 GENERAL D4.1.1 CORRELATION FORM 5-1
5.2 D4.1.1 CPR CORRELATION 5-2
5.2.1 Correlation 5-2
5.2.2 Sub-bundle R-factor for SVEA-96 Optima2 5-7
5.2.3 Determination of D4.1.1 Additive Constants 5-10
5.3 DOUBLE PEAK CORRECTION 5-11
5.4 APPLICATION OF D4.1.1 CORRELATION TO FULL SVEA-96 OPTIMA2 ASSEMBLY 5-13
5.4.1 Mismatch Factor Method 5-14
5.4.2 Sub-bundle Model 5-15
5.4.3 Conservative Assembly CPR Based on Sub-bundle CPR 5-17

6 CORRELATION EVALUATION 6-1
6.1 D4.1.1 PERFORMANCE RELATIVE TO THE SVEA-96 DATA BASE 6-1
6.2 CORRELATION UNCERTAINTY AND RANGE OF THE CORRELATION 6-4

TABLE OF CONTENTS (cont.)

7 CONFIRMATION FOR TRANSIENT APPLICATION 7-1
7.1 INTRODUCTION 7-1
7.2 TRANSIENT IMPLEMENTATION VALIDATION METHODOLOGY 7-1
7.3 TRANSIENT DRYOUT EXPERIMENTS 7-2
7.3.1 FRIGG Loop 7-2
7.3.2 Test Section 7-2
7.3.3 Transient Tests Description 7-3
7.3.4 Dryout Threshold Temperature 7-4
7.3.5 Transient Data 7-4
7.4 IMPLEMENTATION VALIDATION FOR BISON CODE 7-5
7.4.1 BISON Code 7-5
7.4.2 BISON Model 7-6
7.4.3 BISON Test Simulation Results 7-6
7.5 SUMMARY 7-7

8 CONCLUSIONS 8-1

9 REFERENCES 9-1

APPENDIX A SVEA-96 OPTIMA2 ASSEMBLY DESCRIPTION A-1

APPENDIX B SVEA 96 OPTIMA2 STEADY STATE CRITICAL POWER TEST DATA COSINE-PEAKED AXIAL POWER SHAPE B-1

APPENDIX C SVEA 96 OPTIMA2 STEADY STATE CRITICAL POWER TEST DATA BOTTOM-PEAKED AXIAL POWER SHAPE C-1

APPENDIX D SVEA 96 OPTIMA2 STEADY STATE CRITICAL POWER TEST DATA TOP-PEAKED AXIAL POWER SHAPE D-1

LIST OF TABLES

Table 3.1 Cosine Axial Power Profile 3-7

Table 3.2 Bottom-Peaked Axial Power Profile 3-8

Table 3.3 Top-Peaked Axial Power Profile 3-9

Table 4.1 Number of Points in SVEA-96 Optima2 Test Series 4-8

Table 4.2 Range of Test Parameters 4-8

Table 4.3 Number of Data Points in Various Parameter Ranges (All Three Axial Power Shapes) 4-9

Table 4.4 Number of Data Points in Various Parameter Ranges (Cosine Axial Power Shapes) 4-9

Table 4.5 Number of Data Points in Various Parameter Ranges (Bottom-Peaked Axial Power Shapes) 4-10

Table 4.6 Number of Data Points in Various Parameter Ranges (Top-Peaked Axial Power Shapes) 4-10

Table 4.7 Range of Parameters 4-11

Table 4.8 Examples of Test Reproducibility 4-11

Table 6.1 Number of Data Points and Local Power Distributions (Evaluation Data Set) 6-5

Table 6.2 Number of Data Points and Local Power Distributions (Validation Data Set) 6-5

Table 6.3 Mean Prediction Errors and Standard Deviations for D4.1.1 CPR Correlation 6-5

Table 6.4 Number and Percent of Calculated Data Points Exceeding the 5% Boundary 6-6

Table 6.5 Mean Prediction Error and Standard Deviations for D4.1.1 CPR Correlation for Data Ranges 6-6

Table 6.6 Mean and Standard Deviations in Mean Prediction Error for Various Mass Flux Ranges 6-7

Table 6.7 Range of Validity of D4.1.1 6-7

Table 7.1a SF24SB – Test Matrix for Power Increase Transients with Bottom-Peaked Axial Power Shape 7-8

Table 7.1b SF24SB – Test Matrix for Flow Decrease Transients with Bottom-Peaked Axial Power Shape 7-8

Table 7.2a SF24S – Test Matrix for Power Increase Transients with Cosine Axial Power Shape 7-9

Table 7.2b SF24S – Test Matrix for Flow Decrease Transients with Cosine Axial Power Shape 7-9

LIST OF TABLES (cont.)

Table 7.3a	SF24ST – Test Matrix for Power Increase Transients with Top-Peaked Axial Power Shape	7-10
Table 7.3b	SF24ST – Test Matrix for Flow Decrease Transients with Top-Peaked Axial Power Shape	7-10
Table 7.4	SF24SB – Bottom-Peaked Test Results and BISON/SLAVE Predictions	7-11
Table 7.5	SF24S – Cosine Test Results and BISON/SLAVE Predictions	7-16
Table 7.6	SF24ST – Top-Peaked Test Results and BISON/SLAVE Predictions	7-21
Table 7.7	Criteria for Non-Conservative Prediction of Tranient CPR Prediction	7-23

LIST OF FIGURES

Figure 3.1 FRIGG Loop Diagram 3-10

Figure 3.2 Axial Positions of Spacers and Pressure Taps 3-11

Figure 3.3 Test Sections Data and Numbering of Rods in the FRIGG Loop 3-12

Figure 3.4 Axial Power Shape Used in the FRIGG Test (Cosine, Bottom and Top) 3-13

Figure 3.5 Heater Rod Design 3-14

Figure 3.6 Part-Length Heater Rod Design 3-15

Figure 3.7 Rod Types and Axial Positions of Spacers and Thermocouples in the Cosine Test 3-16

Figure 3.8 Rod Types and Axial Positions of Spacers and Thermocouples in the Bottom Test 3-17

Figure 3.9 Rod Types and Axial Positions of Spacers and Thermocouples in the Top Test 3-18

Figure 3.10 Data Acquisition System 3-19

Figure 4.1a Histogram for all SVEA-96 Optima2 Tests, Frequency Versus Mass Flux 4-12

Figure 4.2a Histogram from all SVEA-96 Optima2 Tests, Frequency Versus Pressure 4-12

Figure 4.3a Histogram from all SVEA-96 Optima2 Tests, Frequency Versus Subcooling 4-13

Figure 4.4a Histogram from all SVEA-96 Optima2 Tests, Frequency Versus R-factor 4-13

Figure 4.1b Histogram from SVEA-96 Optima2 Tests, Frequency Versus Mass Flux (Cosine Axial Power Shape) 4-14

Figure 4.2b Histogram from SVEA-96 Optima2 Tests, Frequency Versus Pressure (Cosine Axial Power Shape) 4-14

Figure 4.3b Histogram from SVEA-96 Optima2 Tests, Frequency Versus Subcooling (Cosine Axial Power Shape) 4-15

Figure 4.4b Histogram from SVEA-96 Optima2 Tests, Frequency Versus R-factor (Cosine Axial Power Shape) 4-15

Figure 4.1c Histogram from SVEA-96 Optima2 Tests, Frequency Versus Mass Flux (Bottom-Peaked Axial Power Shape) 4-16

Figure 4.2c Histogram from SVEA-96 Optima2 Tests, Frequency Versus Pressure (Bottom-Peaked Axial Power Shape) 4-16

Figure 4.3c Histogram from SVEA-96 Optima2 Tests, Frequency Versus Subcooling (Bottom-Peaked Axial Power Shape) 4-17

Figure 4.4c Histogram from SVEA-96 Optima2 Tests, Frequency Versus R-factor (Bottom-Peaked Axial Power Shape) 4-17

Figure 4.1d Histogram from SVEA-96 Optima2 Tests, Frequency Versus Mass Flux (Top-Peaked Axial Power Shape) 4-18

LIST OF FIGURES (cont.)

Figure 4.2d Histogram from SVEA-96 Optima2 Tests, Frequency Versus Pressure (Top-Peaked Axial Power Shape) 4-18

Figure 4.3d Histogram from SVEA-96 Optima2 Tests, Frequency Versus Subcooling (Top-Peaked Axial Power Shape) 4-19

Figure 4.4d Histogram from SVEA-96 Optima2 Tests, Frequency Versus R-factor (Top-Peaked Axial Power Shape) 4-19

Figure 4.5 Range of Test Parameters (Pressure vs. Mass Flux) Compared with Typical Application Range 4-20

Figure 4.6 Range of Test Parameters (Pressure vs. Subcooling) Compared with Typical Application Range 4-21

Figure 4.7 Range of Test Parameters (Subcooling vs. Mass Flux) Compared with Typical Application Range 4-22

Figure 4.8 Range of Test Parameters (R-factor vs. Mass Flux) Compared with Typical Application Range 4-23

Figure 4.9 Critical Power Versus Flow at 70 Bar, 10 K Subcooling, for Uniform Local Power Distribution 4-24

Figure 4.10 Critical Power Versus Flow at 70 Bar, 10 K Subcooling, for Optimized Local Power Distribution 4-25

Figure 4.11 SF24S Critical Power Versus Subcooling at 70 Bar, Uniform Local Power Distribution, for Various Flows 4-26

Figure 4.12 SF24S Critical Power Versus Subcooling at 70 Bar, Optimized Local Power Distribution, for Various Flows 4-26

Figure 4.13 SF24S Critical Power Versus Pressure at 10 K Subcooling, Uniform Local Power Distribution, for Various Flows 4-27

Figure 4.14 SF24S Critical Power Versus Pressure at 20 K Subcooling, Uniform Local Power Distribution, for Various Flows 4-27

Figure 4.15 SF24S Critical Power Versus Pressure at 30 K Subcooling, Uniform Local Power Distribution, for Various Flows 4-28

Figure 4.16 SF24S Critical Power Versus Pressure at 40 K Subcooling, Uniform Local Power Distribution, for Various Flows 4-28

Figure 4.17 SF24S Critical Power Versus Pressure at 10 K Subcooling, Optimized Local Power Distribution, for Various Flows 4-29

Figure 4.18 SF24S Critical Power Versus Pressure at 20 K Subcooling, Optimized Local Power Distribution, for Various Flows 4-29

LIST OF FIGURES (cont.)

Figure 4.19 SF24SB Critical Power Versus Subcooling at 70 bar, Uniform Local Power Distribution, for Various Flows 4-30

Figure 4.20 SF24SB Critical Power Versus Subcooling at 70 bar, Optimized Local Power Distribution, for Various Flows 4-30

Figure 4.21 SF24SB Critical Power Versus Pressure at 10 K Subcooling, Uniform Local Power Distribution, for Various Flows 4-31

Figure 4.22 SF24SB Critical Power Versus Pressure at 20 K Subcooling, Uniform Local Power Distribution, for Various Flows 4-31

Figure 4.23 SF24SB Critical Power Versus Pressure at 40 K Subcooling, Uniform Local Power Distribution, for Various Flows 4-32

Figure 4.24 SF24SB Critical Power Versus Pressure at 10 K Subcooling, Optimized Local Power Distribution, for Various Flows 4-32

Figure 4.25 SF24SB Critical Power Versus Pressure at 20 K Subcooling, Optimized Local Power Distribution, for Various Flows 4-33

Figure 4.26 SF24ST Critical Power Versus Subcooling at 70 Bar, Uniform Local Power Distribution, for Various Flows 4-33

Figure 4.27 SF24ST Critical Power Versus Subcooling at 70 Bar, Optimized Local Power Distribution, for Various Flows 4-34

Figure 4.28 SF24ST Critical Power Versus Pressure at 10 K Subcooling Uniform Local Power Distribution, for Various Flows 4-34

Figure 4.29 SF24ST Critical Power Versus Pressure at 20 K Subcooling, Uniform Local Power Distribution, for Various Flows 4-35

Figure 4.30 SF24ST Critical Power Versus Pressure at 40 K Subcooling, Uniform Local Power Distribution, for Various Flows 4-35

Figure 4.31 SF24ST Critical Power Versus Pressure at 10 K Subcooling Optimized Local Power Distribution, for Various Flows 4-36

Figure 4.32 SF24ST Critical Power Versus Pressure at 20 K Subcooling, Optimized Local Power Distribution, for Various Flows 4-36

Figure 5.1 The X_G, X_B, X_P and X_A Functions 5-19

Figure 5.2 The $X_{G,P}$, $X_{G,B}$, $X_{P,A}$, $X_{B,A}$, and $X_{A,G}$ Functions 5-19

Figure 5.3 The Linear Term and Cross Term in CFR Defined in Section 5.2.1 (i.e., $f(RN) = -82.9 \cdot 10^{-3} \cdot RN$ and $f(RN*GN) = -0.75 \cdot 10^{-3} \cdot RN \cdot GN$) 5-20

Figure 5.4 Rod Index 5-20

Figure 5.5 SVEA-96 Optima2 Additive Constants 5-21

LIST OF FIGURES (cont.)

Figure 5.6 MF_s as a Function of Relative Sub-bundle Power....5-21

Figure 5.7 Example of Axial Shapes Defining Correction Factor....5-22

Figure 6.1 D4.1.1 Predicted Versus Measured Critical Power for all Data Points – the Lines Represent ±5% Error....6-8

Figure 6.2 D4.1.1 Prediction Error as a Function of Mass Flux for all Data Points....6-8

Figure 6.3 D4.1.1 Prediction Error as a Function of Mass Flux for Validation Data....6-9

Figure 6.4 D4.1.1 Prediction Error as a Function of Outlet Pressure for all Data Points....6-9

Figure 6.5 D4.1.1 Prediction Error as a Function of Inlet Subcooling for all Data Points....6-10

Figure 6.6 D4.1.1 Prediction Error as a Function of Boiling Length for all Data Points....6-10

Figure 6.7 D4.1.1 Prediction Error as a Function of Annular Flow Length for all Data Points....6-11

Figure 6.8 D4.1.1 Prediction Error as a Function of R-factor for all Data Points....6-11

Figure 6.9 D4.1.1 for all Test Data – Histogram of Frequency Versus CPR Error....6-12

Figure 6.10 D4.1.1 Critical Power Dependence on Axial Power Shape (Pressure = 70 bar, Subcooling = 10K, R-factor = 0.93)....6-12

Figure 6.11 D4.1.1 Critical Power Dependence on Subcooling....6-13

Figure 6.12 Mean Prediction Error as a Function of Mass Flux – Cosine Axial Power Profile....6-14

Figure 6.13 Mean Prediction Error as a Function of Mass Flux – Bottom-Peaked Axial Power Profile....6-15

Figure 6.14 Mean Prediction Error as a Function of Mass Flux – Top-Peaked Axial Power Profile....6-16

Figure 6.15 Prediction Error Versus Mass Flux at 35 Bar....6-17

Figure 6.16 Prediction Error Versus Mass Flux at 70 Bar....6-18

Figure 6.17 Prediction Error Versus Mass Flux at 80 Bar....6-19

Figure 6.18 Prediction Error Versus Subcooling at 35 Bar....6-20

Figure 6.19 Prediction Error Versus Subcooling at 70 Bar....6-21

Figure 6.20 Prediction Error Versus Subcooling at 80 Bar....6-22

Figure 6.21 Prediction Error Versus Mass Flux at 10 Degree C Subcooling....6-23

Figure 6.22 Prediction Error Versus Mass Flux at 20 Degree C Subcooling....6-24

Figure 6.23 Prediction Error Versus Mass Flux at 40 Degree C Subcooling....6-25

Figure 6.24 Prediction Error Versus Mass Flux for an R-factor of 0.91....6-26

Figure 6.25 Prediction Error Versus Mass Flux for an R-factor of 0.93....6-27

LIST OF FIGURES (cont.)

Figure 6.26 Prediction Error Versus Mass Flux for an R-factor of 0.95 6-28

Figure 6.27 Prediction Error Versus Pressure for an R-factor of 0.91 6-29

Figure 6.28 Prediction Error Versus Pressure for an R-factor of 0.93 6-30

Figure 6.29 Prediction Error Versus Pressure for an R-factor of 0.95 6-31

Figure 6.30 Prediction Error Versus Subcooling for an R-factor of 0.91 6-32

Figure 6.31 Prediction Error Versus Subcooling for an R-factor of 0.93 6-33

Figure 6.32 Prediction Error Versus Subcooling for an R-factor of 0.95 6-34

Figure 7.1a Power Profiles 7-24

Figure 7.1b Power Profiles Used for Power Transients 7-24

Figure 7.1c Power Profiles Used for Power Transients 7-25

Figure 7.1d Power Profiles Used for Power Transients 7-25

Figure 7.2a Flow Profiles Used for Flow Reduction Transients 7-26

Figure 7.2b Flow Profiles 7-26

Figure 7.2c Flow Profiles 7-27

Figure 7.3a Power Increase Transient – Power and Mass Flux as Function of Time Experiment Number 1391 7-27

Figure 7.3b Power Increase Transient – Measured Temperature – Experiment Number 1391 7-28

Figure 7.4a Power Increase Transient (Slow) – Power and Mass Flux as Function of Time Experiment number 1446 7-28

Figure 7.4b Power Increase Transient (Slow) – Measured Temperature – Experiment Number 1446 7-29

Figure 7.5a Flow Reduction Transient – Power and Mass Flux as Function of Time Experiment Number 1414 7-29

Figure 7.5b Flow Reduction Transient – Measured Temperature – Experiment Number 1414 7-30

Figure 7.6 BISON-SLAVE Model for Test Heater Rod 7-31

Figure 7.7 Transient Validation for SF24SB – Bottom-Peaked Axial Power Shape 7-32

Figure 7.8 Transient validation for SF24S – Cosine Axial Power Shape 7-32

Figure 7.9 Transient Validation for SF24ST – Top-Peaked Axial Power Shape 7-33

Figure 7.10 Measured Time to Boiling Transition vs. Predicted Time 7-33

1 SUMMARY

This report describes the development of the Critical Power Ratio (CPR) correlation for Westinghouse SVEA-96 Optima2 BWR fuel assemblies. The CPR correlation for SVEA-96 Optima2 fuel is referred to as D4.1.1. Development of the D4.1.1 CPR correlation is a continuation of the process to establish CPR correlations of the same general form for Westinghouse 10x10 SVEA fuel. CPR correlations based on full sets of critical power data have previously been established for the SVEA-96, SVEA-96+, and SVEA-96 Optima designs. The NRC has previously reviewed and accepted the ABBD1.0 and ABBD2.0 CPR correlations for SVEA-96 and SVEA-96+ fuel, respectively, as discussed in References 1 and 2. Westinghouse does not intend to offer the SVEA-96 Optima assembly in the U.S. Therefore, the CPR correlation for SVEA-96 Optima design will not be submitted to the NRC.

The D4.1.1 CPR correlation for the SVEA-96 Optima2 assembly and the bases for its acceptance are presented in this report. NRC review and acceptance of the D4.1.1 correlation for licensing applications is requested.

The D4.1.1 CPR correlation has the same general form as the ABBD1.0 and ABBD2.0 correlations documented in References 1 and 2 in that the SVEA-96 Optima2 data were correlated by adapting a critical power correlation of the critical quality/boiling length form [

]^{a,c}. However, several improvements have been introduced in the D4.1.1 CPR correlation relative to the ABBD1.0 and ABBD2.0 correlations. In general, these features have been introduced to more effectively capture the physical characteristics of the dryout phenomenon as well as observed trends in CPR in the correlation form prior to adjusting appropriate correlation constants to fit the Critical Power data. These improved features can be summarized as follows:

[

]^{a,c}

Reference 3 describes the application of the improvements identified as items 1 and 3 above to the ABBD1.0 and ABBD2.0 CPR correlations described in References 1 and 2. Reference 3 is currently under review at the NRC.

Three different test series have been performed to support the SVEA-96 Optima2 CPR correlation development. These test series utilized 24-rod SVEA-96 Optima2 sub-bundles with three different axial

power shapes. The tests include measurements of critical power at pressures between [ ]^{a,c} bar and an inlet subcooling temperature range between [ ]^{a,c}. The mass flux range in the tests is [ ]^{a,c} kg/(m^{2}s). The critical power measurements were performed for [ ]^{a,c} different local power distributions to capture the influence on critical power of various local peaking factors and various peak power rod locations.

The D4.1.1 correlation predicts the measured critical powers over the entire database with a mean error of [ ]^{a,c} and a standard deviation of [ ]^{a,c}.

2 INTRODUCTION

This report describes the development and qualification of the CPR correlation for the latest generation of SVEA-96 water cross BWR fuel. This fuel is referred to as "SVEA-96 Optima2." The SVEA-96 Optima2 fuel assembly is similar to the SVEA-96 and SVEA-96+ assemblies. These fuel assemblies, (SVEA-96, SVEA-96+ and SVEA-96 Optima2), are composed of four sub-bundles in a 5x5 lattice configuration with one fuel rod missing. A description of the SVEA-96 Optima2 design is provided in Appendix A.

The incentive for developing the SVEA-96 Optima2 design was to support the current industry move toward higher energy cycles. This goal was accomplished principally by the following enhancements relative to SVEA-96+:

1. improve the nuclear performance primarily by increasing the shut down margin by the introduction of [ ]^{a,c} part length rods (PRLs), and

2. improve the dryout performance by introducing an improved spacer design [ ]^{a,c}.

Each of the four sub-bundles of the SVEA-96 Optima2 consists of 24 fuel rods in a 5X5-1 lattice. [

]^{a,c} A description of the SVEA-96 Optima2 design is provided in Appendix A.

The test sections consist of 24-rod bundles very closely simulating SVEA-96 Optima2 fuel sub-bundles operated in BWRs. Indirectly heated rods connected to several individual rectifier units make it possible to control the local power (i.e., relative rod power) distribution in a simple way and test a wide range of local power distributions. The objectives of these tests and the CPR evaluation program were as follows:

1. Determine the steady state critical power capability of the SVEA-96 Optima2 assembly over a wide range of simulated BWR operating conditions. The range of BWR operating conditions must be sufficient to provide a Critical Power Ratio (CPR) correlation which will be acceptable for predicting the CPR behavior of the SVEA-96 Optima2 assembly over the entire steady state and transient operating range of BWR's for design and licensing applications.

2. Confirm that the CPR correlation for the SVEA-96 Optima2 assembly (D4.1.1) developed from the steady state critical power data base adequately describes the data base and to establish appropriate biases and uncertainties for licensing applications. Since the correlation was developed from steady state data, it will provide best estimate CPR values for steady state applications. For licensing applications, the correlation will be applied in computer codes accepted by the NRC.

3. Confirm that the CPR correlation for the SVEA-96 Optima2 assembly (D4.1.1) established under steady state conditions provides an adequate description of the change in critical power (ΔCPR) during transient applications. This confirmation is performed by comparing the predictions of the

ABBD2.0 CPR correlation for transient conditions with available transient CPR test data. The Westinghouse methodology for performing this confirmation is illustrated for the BISON-SLAVE code documented in Reference 4.

The test matrix was selected to cover the entire steady state and transient operating range expected for U.S. BWR's and to sufficiently cover off-nominal conditions to allow its application to transient and accident conditions. Particular emphasis has been placed on capturing the dependence on local power distributions within the bundle since this is expected to be the major bundle-specific effect.

The D4.1.1 critical power correlation developed for the SVEA-96 Optima2 assembly is of the critical quality-boiling length form [ ]^{a,c}. It is referred to as the D4.1.1 correlation. The correlation is based on [ ]^{a,c} steady-state critical power points utilizing a full-scale 24-rod bundle. The correlation database contains chopped cosine, top-skewed, and bottom-skewed axial power shapes. The critical power measurements were performed for more than [ ]^{a,c} different local power distributions to capture the influence on critical power of various local peaking factors and various peak power rod locations.

[

]^{a,c}

The degree to which the correlation fits the experimental data is reflected by the average percent deviation of the correlation prediction relative to the measured critical power over the entire data range. The D4.1.1 correlation for SVEA-96 Optima2 fuel predicts the measured critical powers with a mean error of [ ]^{a,c} and a standard deviation of [ ]^{a,c} over the entire steady-state SVEA-96 Optima2 data base.

Conservative transient application of the correlation has been illustrated for implementation of the correlation in the BISON-SLAVE dynamic system transient code. Power increase and flow reduction transient tests were simulated demonstrating conservative prediction of the onset of dryout.

The evaluation in Section 7 provides an illustration using the BISON-SLAVE dynamic code of the Westinghouse methodology for confirming that a CPR correlation based on steady-state data conservatively predicts CPR behavior under transient conditions. This methodology can also be used to confirm that CPR changes during transient events are conservatively treated in other dynamic codes.

3 TEST FACILITY

3.1 DESCRIPTION

The SVEA-96 Optima2 critical power tests were performed in the FRIGG loop in the Westinghouse laboratories in Västerås, Sweden. The FRIGG loop has been utilized for many years to perform thermal hydraulic tests in support of the Westinghouse BWR nuclear program.

A diagram of the FRIGG loop is shown in Figure 3.1. The loop contains a main circulation loop with the test section, a cooling circuit, and a purification system. The head of the main circulation pump can be continuously controlled by means of a variable speed motor. When steam is produced in the test section, the loop pressure is controlled by regulating the cold water flow to spray nozzles in the condenser. Heat is removed by a heat exchanger in the cooling circuit from which water is pumped to the spray nozzles. During start-up and heat balance tests, the loop is filled with water, and the pressure is regulated by balancing the amount of water by means of the feed water pump and a drainage valve. The inlet subcooling is controlled by feeding water from the cooling circuit into the main circulation loop upstream of the pump.

The loop is designed for a maximum pressure of 100 bar and a maximum temperature of 311°C. Carbon steel is used throughout as a construction material, and water quality is carefully controlled. Demineralized and deaerated water is used for filling the loop. Purification is continuous during the tests to keep water quality within specified limits. Normally water conductivity is in the range of 0.15 – 0.30 μS/cm.

3.2 TEST SECTION

The test section consists of a pressure vessel, a Zircaloy flow channel and a SVEA 5x5-1 sub-bundle with 24 heater rods. [

]^{a,c} To avoid deformation at extreme test conditions, the flow channel is reinforced by an outer support structure. Pressure taps are connected to the flow channel at different elevations as shown in Figure 3.2. The pressure transmission lines are brought out of the test section through an instrumentation ring.

An orifice plate is installed at the inlet of the flow channel to provide an even distribution of flow into the channel. The orifice plate has a loss coefficient of five velocity heads, which is close to the lower tie plate loss in standard SVEA-96 Optima2 fuel.

The heated rods are constrained by [ ]^{a,c} of the same type used in the standard reload SVEA-96 Optima2 assembly. Additional Inconel spacers which are not used in the standard SVEA-96 Optima2 are positioned at the inlet and exit of the test section. These additional spacers do not impact the dryout results. The axial locations of the spacers and the pressure taps (DP) are shown in Figure 3.2.

The pressure vessel top flange contains pressure seals similar in design to valve stem packing seals which retain the heater rods in fixed position. The difference in thermal expansion between the heater rods and the pressure vessel is taken care via O-ring pressure seals in the bottom flange.

Dimensions of the test sections are compared with SVEA-96 Optima2 design parameters for a core with 3.81 m active length fuel in Figure 3.3. The design dimensions of the SVEA-96 Optima2 test section which might affect dryout are not identical to those of the standard SVEA-96 Optima2 reload fuel assembly. [

]^{a,c} Therefore, the effects on critical power of the small differences between the SVEA-96 Optima2 sub-bundle test section geometry and the reload fuel assembly dimensions are either negligible or are accounted for in the correlation. It should be noted that minor differences in the flow area of the test sections used for the three axial power shape test series were specifically accounted for in the correlation derivation and evaluation.

The numbers assigned to the heater rods in Figure 3.3 are used to identify the heater rods in Appendices A, B and C. As shown in Figure 3.3, the heater rod numbering scheme identifies the rod location in the sub-bundle.

Tables 3.1 through 3.3 and Figure 3.4 show the axial power shapes used in the three 24-rod sub-bundle test series.

3.3 HEATER RODS

The heater rods used in the tests are indirectly heated. Each heater rod contains a heater element, electrical insulation, Inconel-600 cladding, and [ ]^{a,c}. The heater element is made from a Monel K-500 tube. The heater element terminals consist of a solid nickel transition piece welded to the Monel tube at one end and to a copper electrode brazed to the Monel tube at the other end. The heater-rod non-uniform axial power profiles were generated by laser cutting a spiral on the Monel tube with a variable pitch.

The power rating of the heater rods in the test sections at 380V DC are as follows:

[

]^{a,c}

Sketches of a full-length rod and a cosine-shaped axial power distribution two-third length heater rod are shown in Figures 3.5 and 3.6, respectively.

[

]^{a,c}

[

]^{a,c}

The electrical insulation was machined form solid boron nitrite (BN) pieces. After the BN sleeves were assembled over the heater element, grooves were cut axially to hold the thermocouples in position. Then the heater element assembly was inserted into the oversized Inconel tube used as cladding. The final heater rod dimensions were obtained by swaging the heater assembly to its final dimensions. The swaging operation also provided good contact between the heater element, the insulation material, and the cladding inner surface assuring good heat transfer with low variability from the heating element to the cladding surface.

The thermocouples (dryout detectors) are embedded between the cladding and the insulation sleeves. The full-length rod thermocouple extensions are routed from the top end of the heater rod, and the part-length extensions are routed from the bottom end. The thermocouples used were 0.5 mm unground, Inconel-sheathed, type K, with MgO insulation. The thermocouple wire used was of premium grade. The thermocouple tips were backfilled with BN powder and compacted by swaging to provide a faster response to temperature changes.

Figure 3.7 shows the axial positions of thermocouples in the cosine axial power shape sub-bundle tests. Figure 3.8 shows the axial locations of the thermocouples in the 24-rod sub-bundle bottom peaked axial power shape tests. Figure 3.9 shows the axial positions of the thermocouples in the top peaked axial power shape 24-rod sub-bundle tests. Tables 3.1 through 3.3 show the axial power shapes used in the three 24-rod sub-bundle test series.

It should be noted that in Figures 3.8 and 3.9 [

]^{a,c}

3.4 POWER SUPPLY AND CONTROL

For the sub-bundle tests, electrical power to the heater rods was supplied by a 4.2 MW DC electrical power system operating at 380 V. The system consisted of 10 units (rectifiers). Six of the units were rated at 300 kW each, and four of the units were rated at 600 kW each.

The upgraded FRIGG loop has a very flexible system for connecting the individual heater rods to selected units. This configuration provides the capability to conveniently obtain numerous combinations of relative rod powers by adjusting the computer signals that control the voltage across each unit. It is this capability which allows a thorough determination of sub-channel factors (e.g., R-factors) providing the relative dryout sensitivity of each fuel rod.

3.5 INSTRUMENTATION

The parameters defining the operating conditions during the tests consist of temperature, pressure, flow, differential pressure and bundle power. These variables and the method by which they are monitored are defined as follows:

p (bar) is the pressure at the test section outlet. The pressure is measured with a precision pressure transducer in the test section inlet. Estimated accuracy in the measured pressure is ± 0.5 bar.

ΔT sub (°C) is the inlet subcooling. This parameter is defined as the difference between the saturation temperature at the test section outlet and the test section inlet temperature. The temperatures were measured with type-K premium grade thermocouples for the SVEA-96 Optima2 sub-bundle tests. Estimated accuracy in the measured inlet subcooling is ± 1°C.

Q (kW) is the power provided to the coolant by the rod bundle. The power is obtained by the summation of the power generated by each heater rod. Heater rod power is calculated as the product of measured current through each rod multiplied by the measured voltage drop across the rod group in which the heater rods are connected. Heater rod current is measured by a calibrated precision shunt connected to the ground electrical leads.

The bundle power is obtained by reducing the measured power by 0.4% to account for the heat generated in heater rod extensions at the inlet and outlet. This power is dissipated in the flanges and is not delivered to the coolant. The estimated accuracy in measured bundle power is ± 1% of the reading at power levels typical at dryout.

$G = \dot{m}/A (kg/m^2s)$ is the mass flux. A is the flow area in the test bundle at room temperature. The flow rate, $\dot{m}$, is measured with an orifice plate in the recirculation line. The estimated accuracy in G is 20 kg/m^2s.

The above accuracies in the major variables represent an accuracy (tolerance) in critical power of about ± 2%.

Rosemount differential pressure (D/P) cells, calibrated to an accuracy of ± 0.5% of full scale, were used to measure pressure drops across various part of the bundle and across the main line flow meter. The main line flow meter was equipped with two D/P cells having different ranges in order to minimize the flow measurement error due to errors in differential pressure measurements.

Thermocouples were located at five elevations along the test vessel in order to measure the fluid temperature in the annulus between the pressure vessel and the flow channel (i.e., the temperature in the bundle differential pressure transmission lines).

3.6 DATA ACQUISITION SYSTEM

A typical data acquisition system is shown in Figure 3.10. Signals reflecting important parameters (e.g., temperature, voltage, current differential pressure and mass flow) are connected to HP3852A data loggers. A sampling frequency of 1.0 Hz was used.

In addition to the data collecting function, the computer was also used as a dryout monitor by utilizing software which allows it to recognize a temperature rise over the initial local temperature in up to 120 heater rod thermocouples. In this case the computer identified the channel(s) indicating dryout. Steady state dryout is assumed to occur for a minimum measured temperature rise of 25°C.

In addition to the dryout indication, two additional limits were used to protect the bundle. A temperature rise of 50°C and a temperature above 450°C automatically cause a decrease in bundle power of 25%. A temperature rise of 75°C causes the bundle power to be shut off completely.

The dryout monitoring function must be in operation before power is provided to the test section. When dryout was detected, the loop conditions were kept constant for about 20 seconds to clearly define average loop conditions at dryout for that test point.

3.7 CRITICAL POWER TESTING PROCEDURE

The measuring instruments used and the data acquisition system are discussed in Sections 3.5 and 3.6. The tests were recorded in blocks of a maximum size of 2400 samples of each parameter, which corresponds to 2400 seconds at a sampling frequency of 1 Hz. Each block generally included several critical power measurements at different mass flows.

The procedure for establishing critical power was as follows:

1. The test identification number was entered into the computer.

2. The target local power distribution was entered into the computer, which established the corresponding rectifier settings.

3. The target bundle inlet subcooling temperature, system pressure, and mass flux were established.

4. The bundle power was slowly increased in small steps. The power was increased until a temperature excursion exceeding 25°C occurred and triggered an alarm. All the thermocouples

were connected to the data loggers, and their outputs recorded during the test. In addition, selected thermocouple outputs were displayed on a monitor in the control room.

Table 3.1 Cosine Axial Power Profile

a,c

Notes:
1. BHL = Bottom of Heated Length (See Figure 3.2)
2. The energy generated in the one-third length rod below the test bundle BHL was added to the first node.

Table 3.2 Bottom-Peaked Axial Power Profile

a,c

Notes:
1. BHL = Bottom of Heated Length (See Figure 3.2)
2. The energy generated in the one-third length rod below the test bundle BHL was added to the first node.

Table 3.3 Top-Peaked Axial Power Profile

a,c

Notes:
1. BHL = Bottom of Heated Length (See Figure 3.2)
2. The energy generated in the one-third length rod below the test bundle BHL was added to the first node.

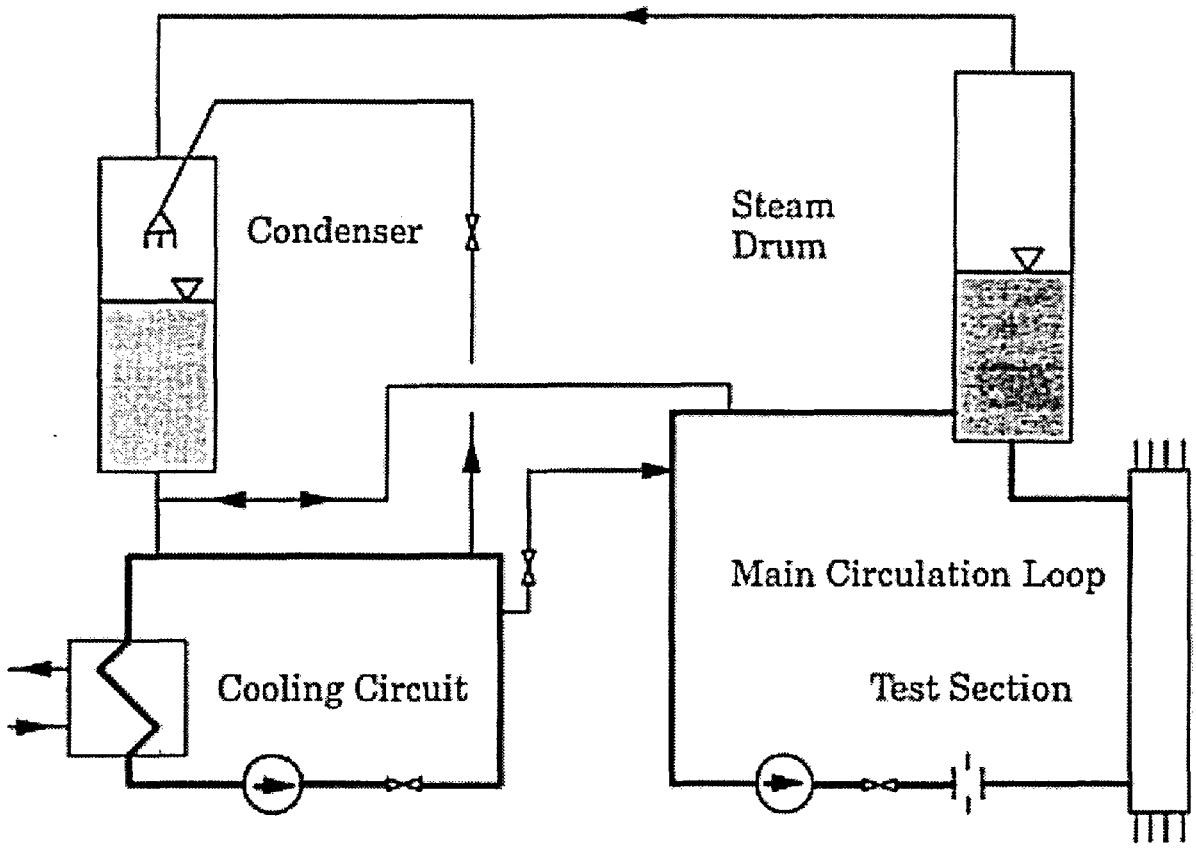

Figure 3.1 FRIGG Loop Diagram

a,c

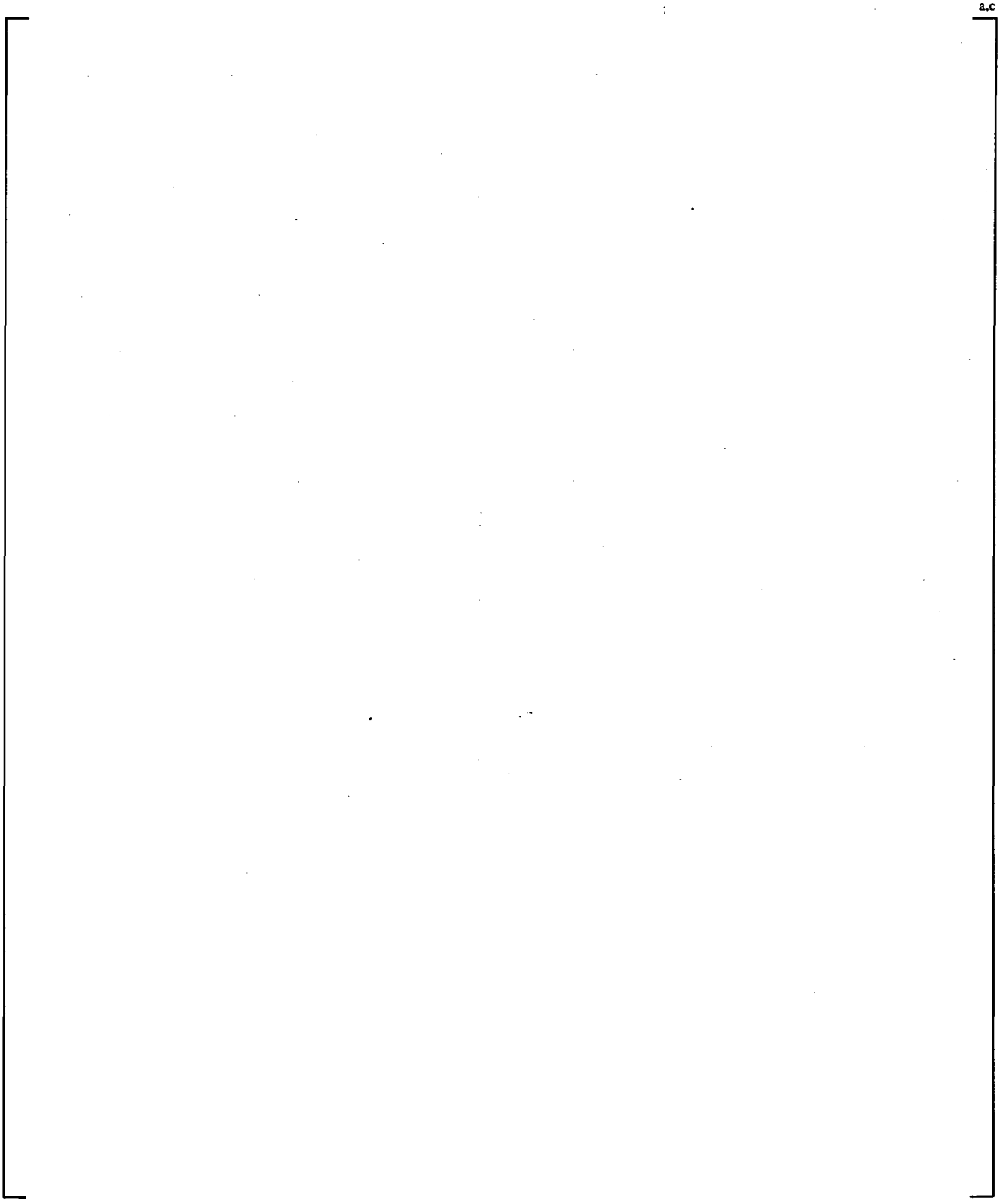

EHL – End of Heated Length, BHL – Beginning of Heated Length

Figure 3.2 Axial Positions of Spacers and Pressure Taps

a,c

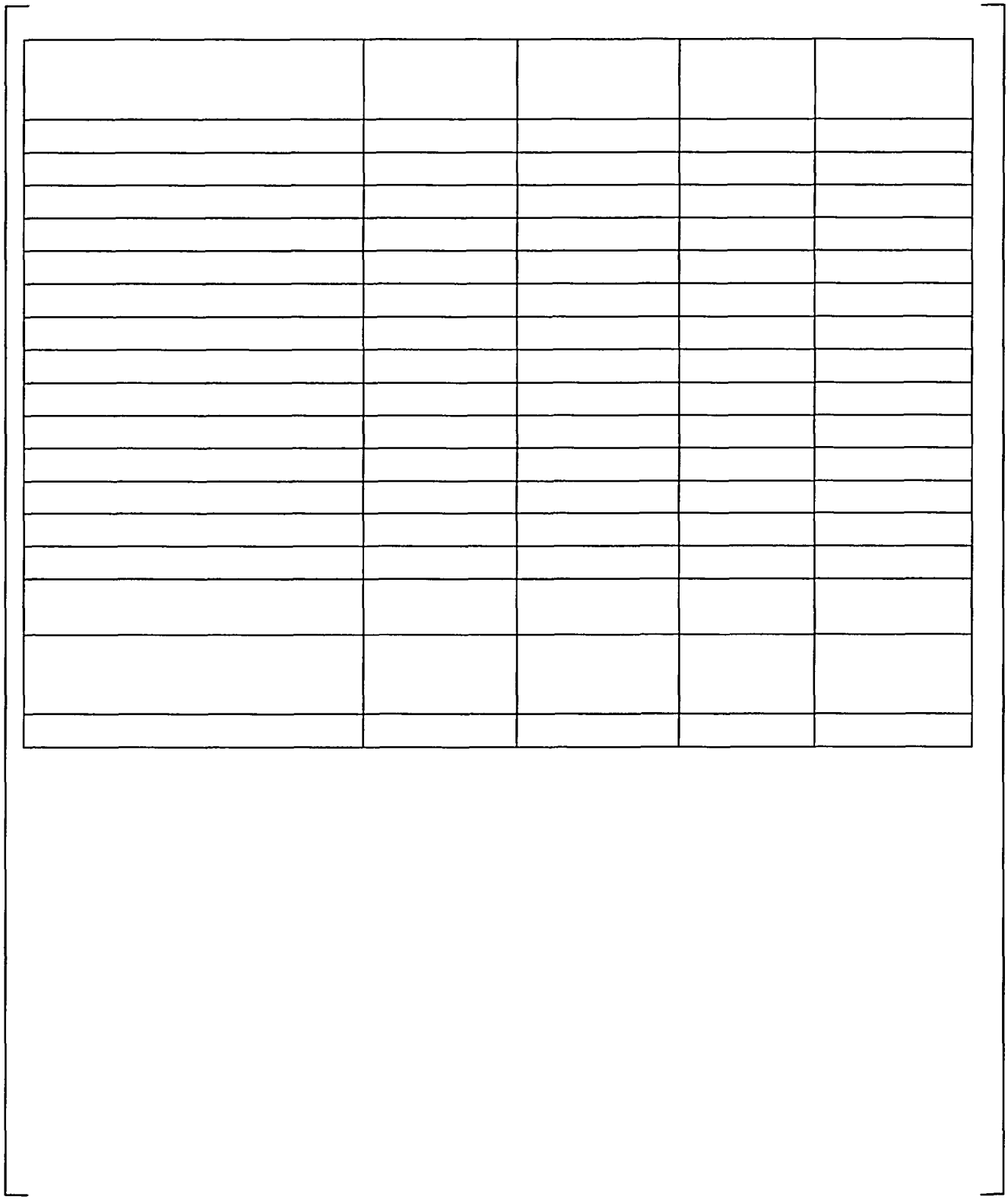

Figure 3.3 Test Sections Data and Numbering of Rods in the FRIGG Loop

a,c

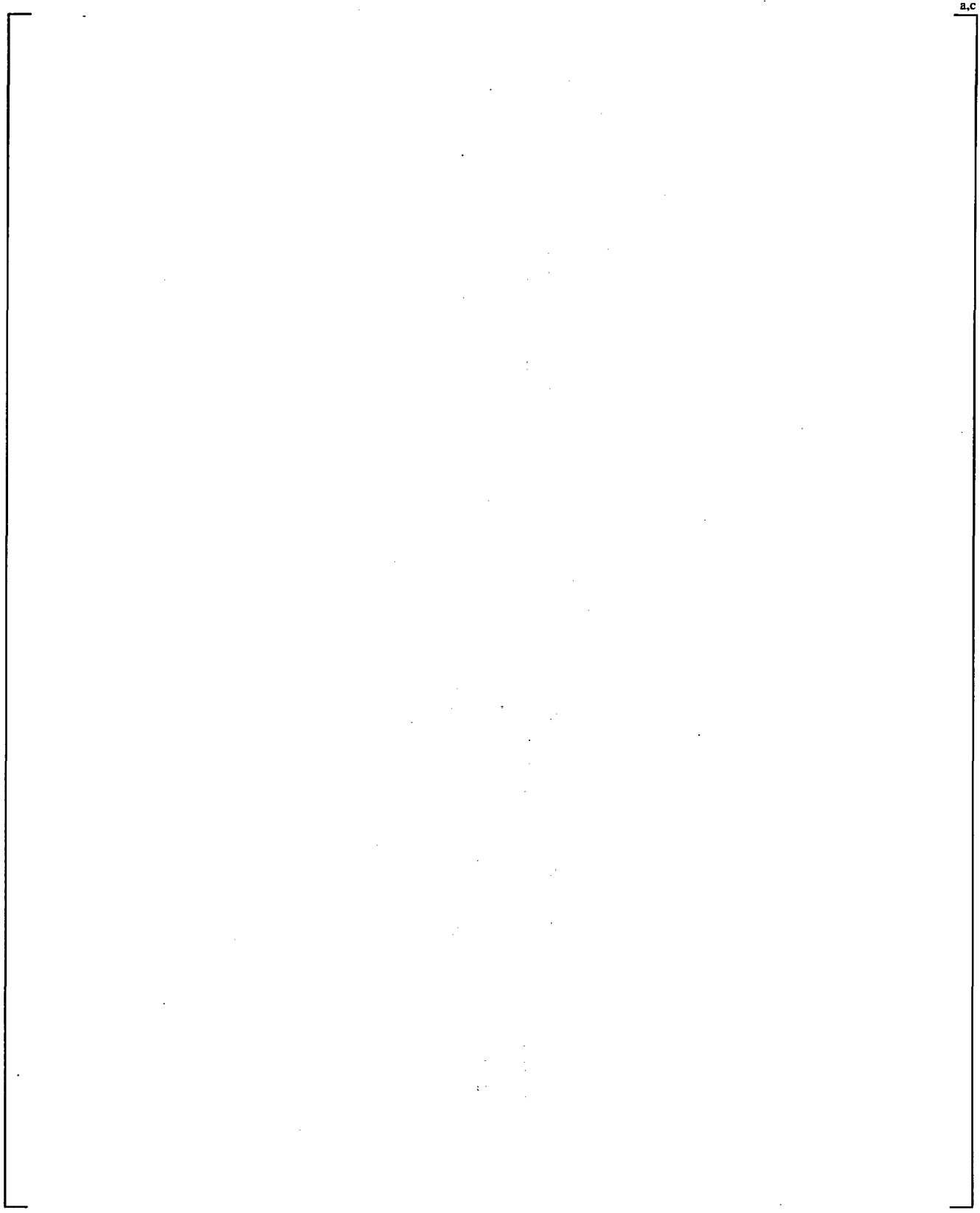

Figure 3.4 Axial Power Shape Used in the FRIGG Test (Cosine, Bottom and Top)

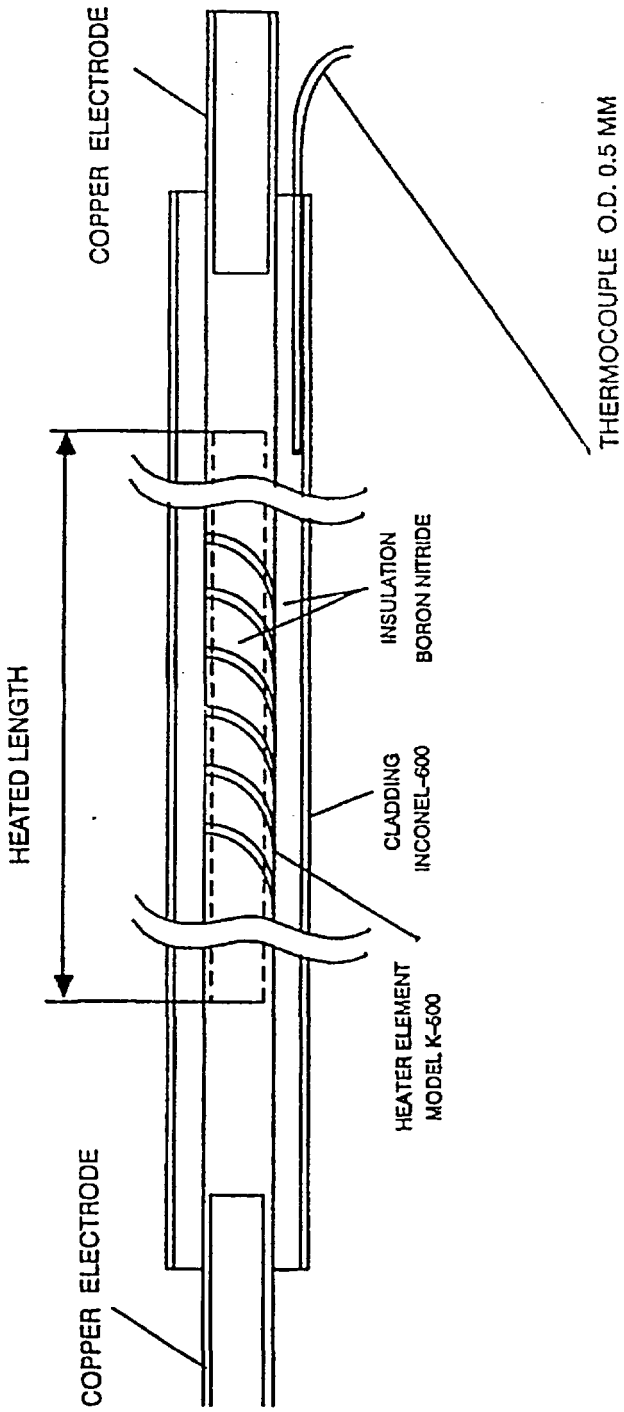

Figure 3.5 Heater Rod Design

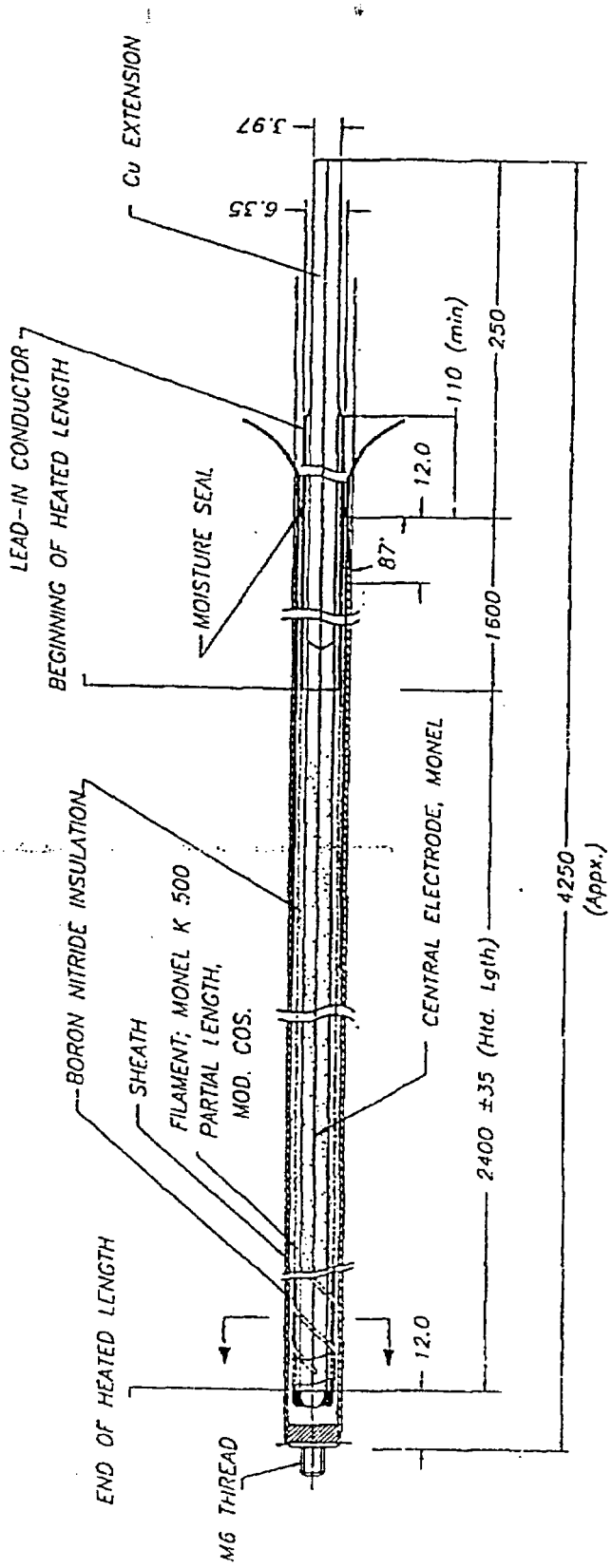

Figure 3.6 Part-Length Heater Rod Design

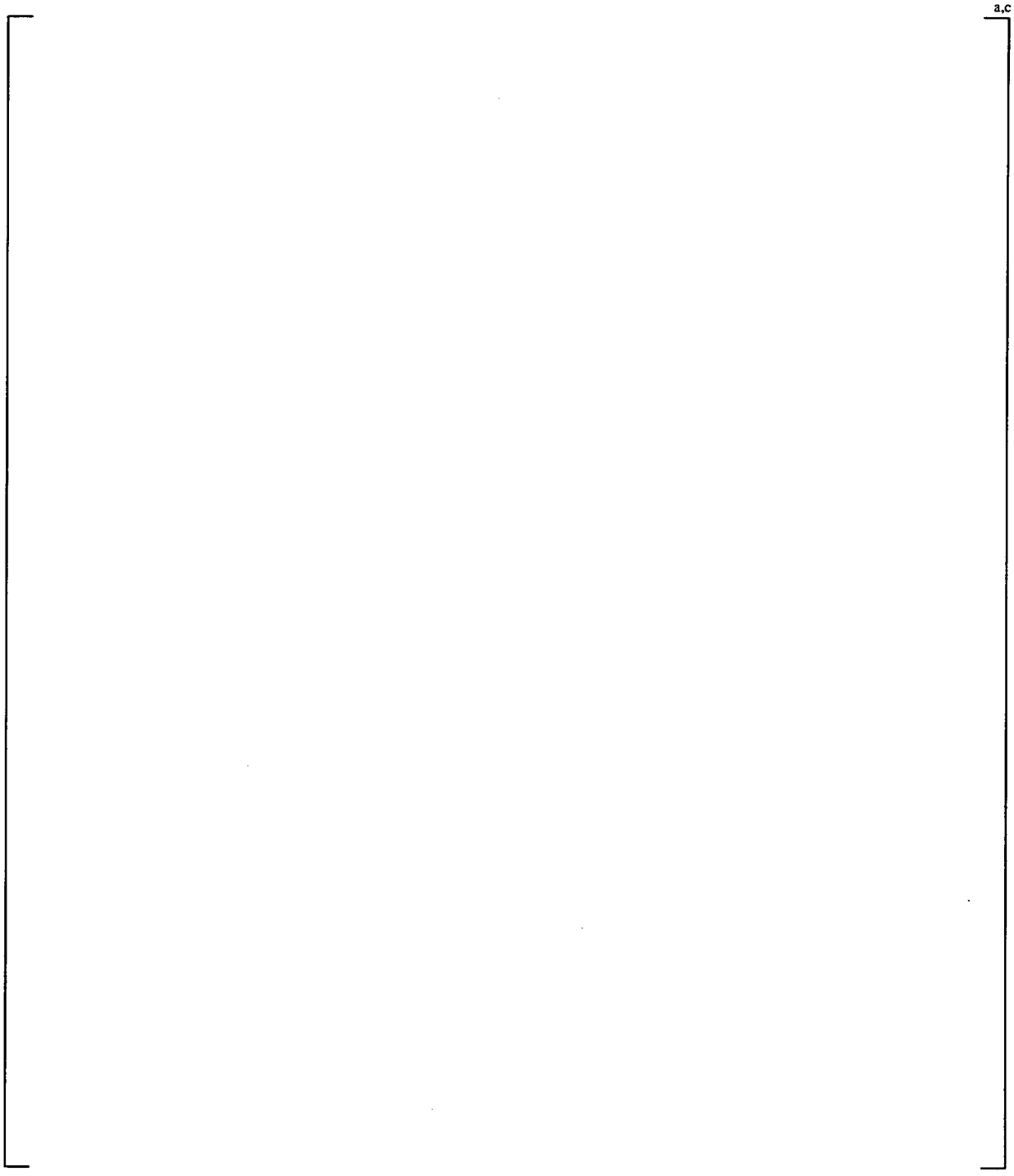

Figure 3.7 Rod Types and Axial Positions of Spacers and Thermocouples in the Cosine Test

a,c

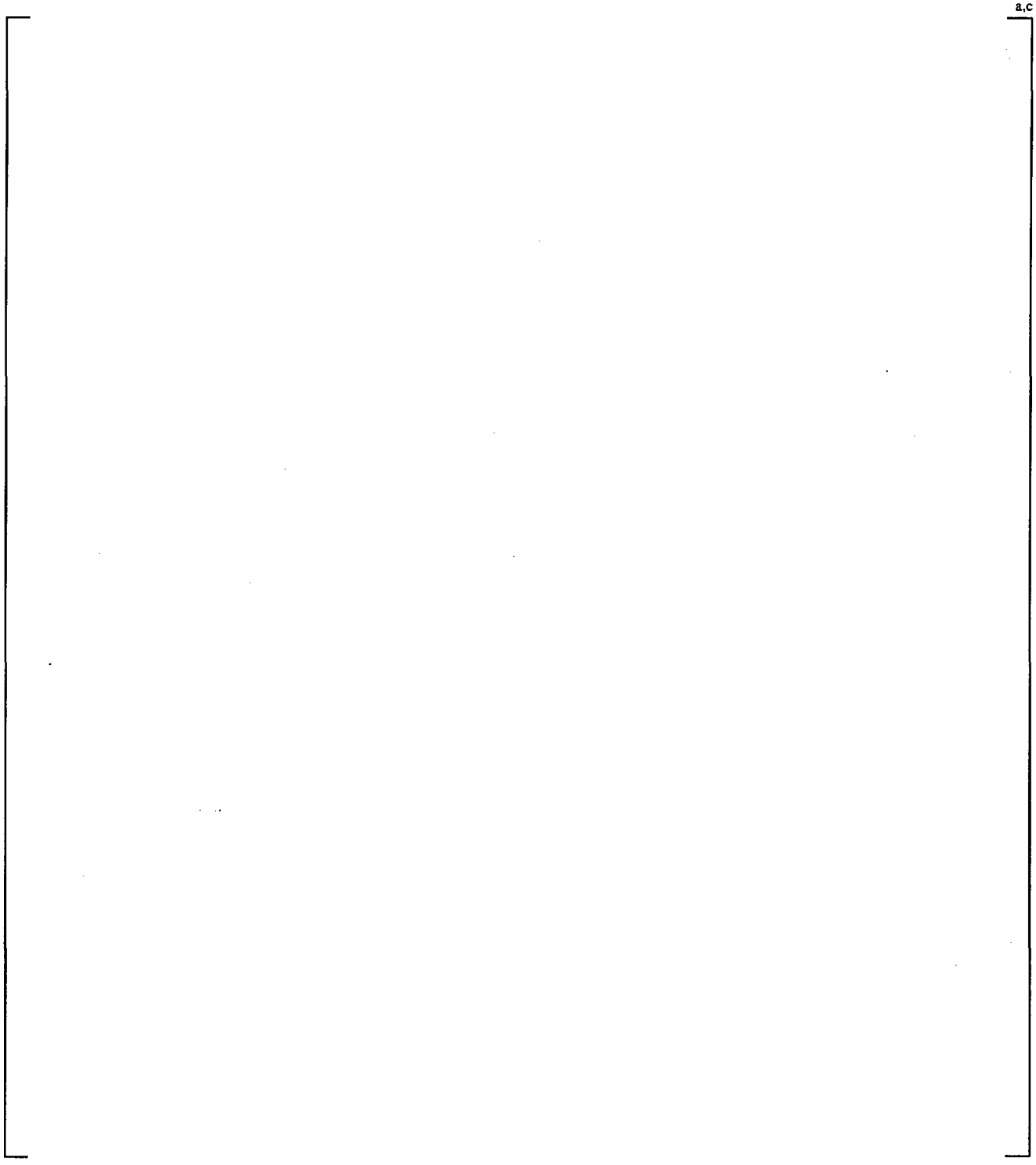

Figure 3.8 Rod Types and Axial Positions of Spacers and Thermocouples in the Bottom Test

a,c

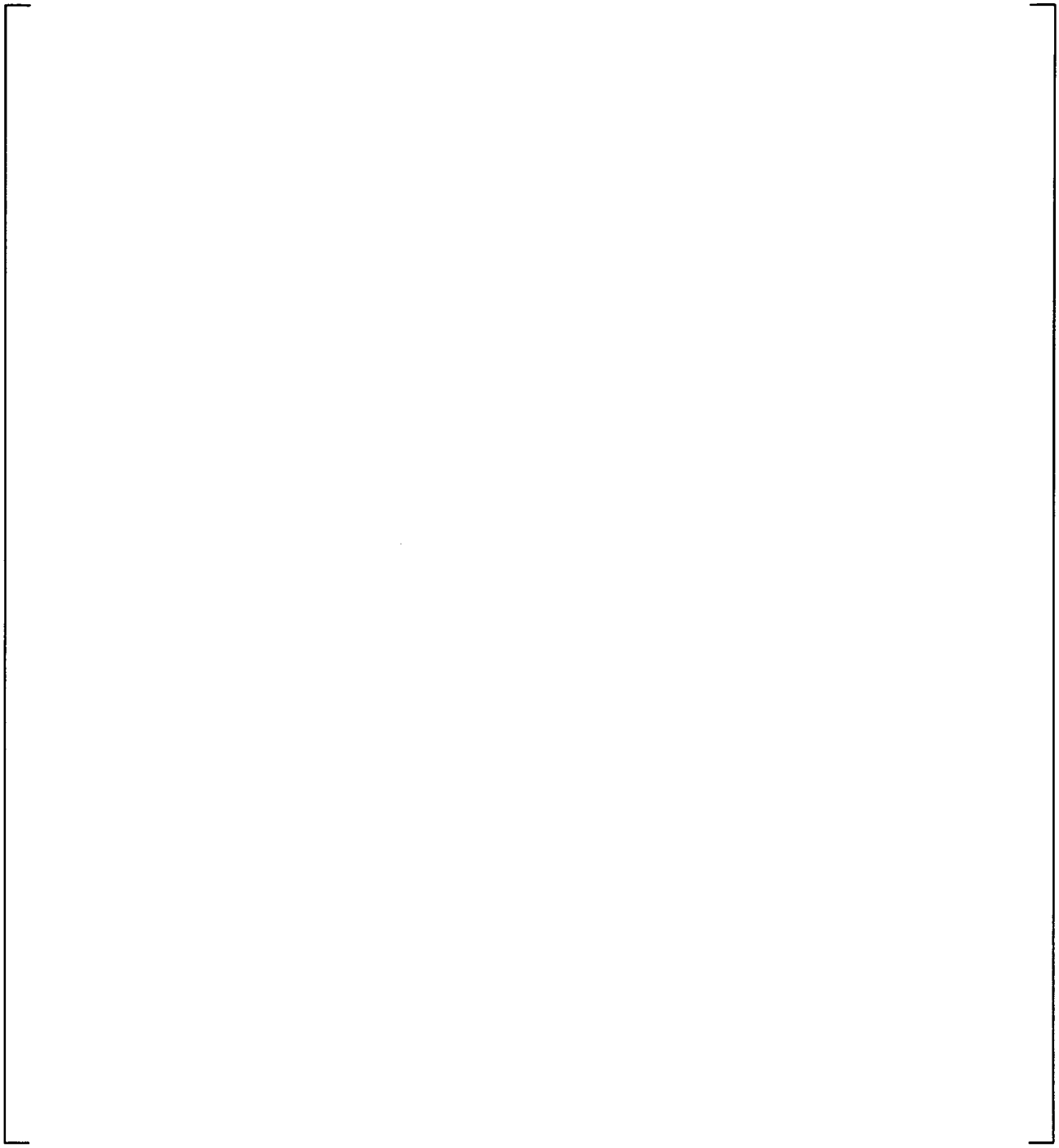

Figure 3.9 Rod Types and Axial Positions of Spacers and Thermocouples in the Top Test

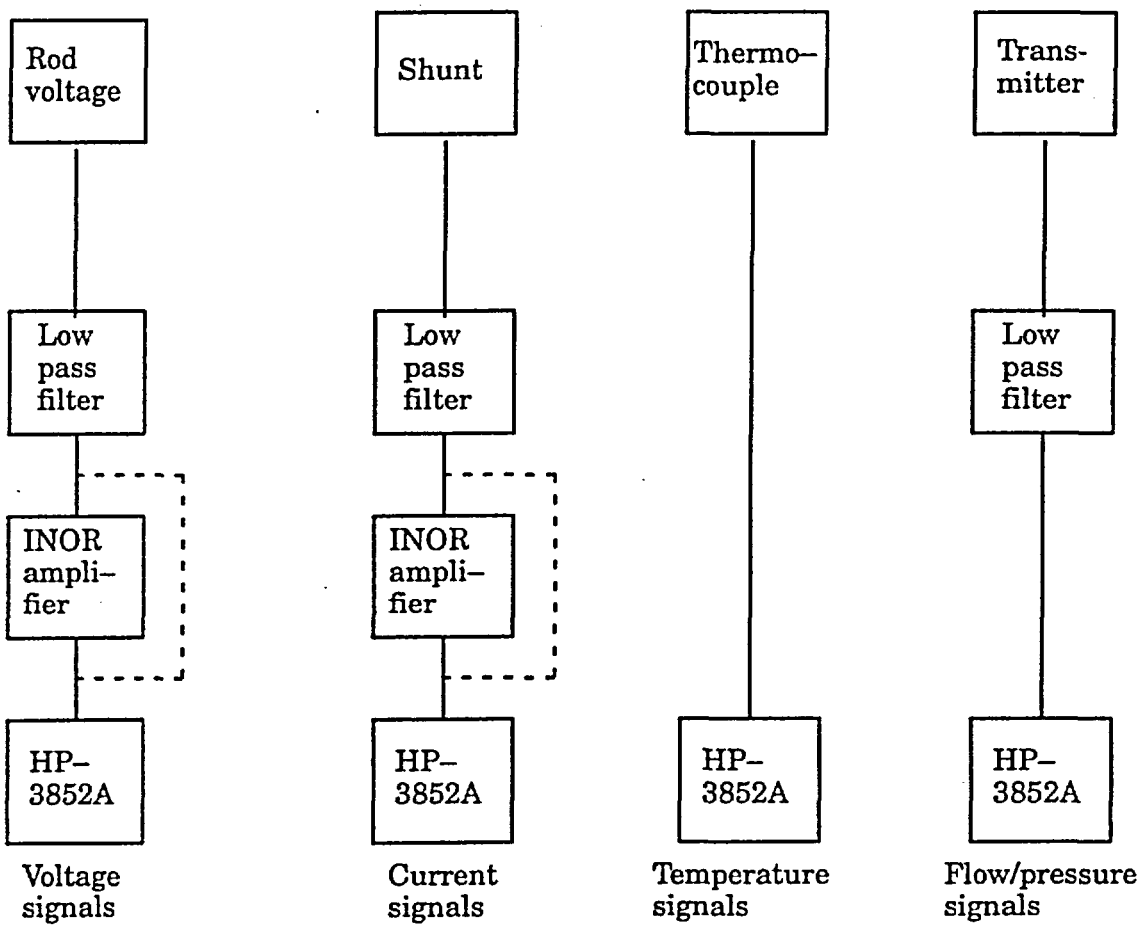

Figure 3.10 Data Acquisition System

4 TEST PROGRAM

As discussed in Section 3, the test program included three separate test series. These series were performed with full-scale SVEA-96 Optima2 24-rod sub-bundle test sections. The three sub-bundle test series differ with respect to the axial power shape provided by the heater rods. Sub-bundle data were obtained for cosine, bottom-peaked, and top-peaked axial power shapes. The test results for the three sub-bundle test series are given in Appendix B (cosine axial power shape), Appendix C (bottom-peaked axial power shape), and Appendix D (top-peaked axial power shape). The test series are identified by the following test identification ranges:

Axial Power Shape	Initial Test Point	Final Test Point	Data Point Table
Cosine	1022-1-AA3	1491-170-MM2	Appendix B
Bottom-Peaked	1017-1-AA3	1276-56-EE11	Appendix C
Top-Peaked	1020-1-AA4	1130-5-DD5	Appendix D

The number of data points and local power distributions in the cosine, bottom-peaked, and top-peaked test series are summarized in Table 4.1. As noted in Appendices B, C and D of this document, the actual local power distribution at which the data point was measured may differ slightly from the nominal distribution. The local power distributions actually measured for each data point, and the R-factor corresponding to that distribution, were used in the correlation derivation and evaluation.

4.1 RANGE OF TEST PARAMETERS

The ranges of test parameters over which the sub-bundle critical power tests were conducted are shown in Table 4.2.

Histograms displaying the ranges of mass flux, pressure, inlet subcooling, and local power distribution as reflected by the CPR correlation R-factor values are shown in Figures 4.1a through 4.1d, 4.2a through 4.2d, 4.3a through 4.3d, and 4.4a through 4.4d, respectively. In each case, the figure denoted "a" is a histogram showing the entire range of data for all three axial power shapes. The figures denoted "b," "c," and "d" identify histograms showing the range of data for the cosine, bottom-peaked, and top-peaked axial power shapes, respectively. The number of data points obtained in each parameter range (mass flux, pressure, inlet subcooling) are shown in Tables 4-3 through 4-6 for all axial power shape tests, the cosine axial power shape tests, bottom-peaked axial power shape tests, and top-peaked axial power shape tests, respectively.

[

]^{a,c}

[

]a,c

4.2 JUSTIFICATION FOR RANGE OF TEST PARAMETERS

The critical power performance of a test bundle is a function of mass flux, system pressure, inlet subcooling, axial power distribution, and local power distribution. The range of the test parameters for which the critical power tests were conducted is presented in Section 4.1. Justification for the ranges is summarized in the following subsections.

4.2.1 Mass Flux

Critical power is a strong function of mass flux. Therefore, data were obtained at numerous points [ ]a,c over the range of mass flux considered to establish the correlation at various values of pressure, inlet subcooling, and bundle local powers.

The mass flux varied from about [ ]a,c. The range of mass flux representing normal operations and AOOs is [ ]a,c. The mass flux points used for the tests cover this expected operating range.

4.2.2 System Pressure

Data were obtained at [

]a,c. This range provided sufficient data to determine the system pressure dependence of critical power over the expected range of application of the correlation. [

]a,c

4.2.3 Inlet Subcooling

It is well known (e.g., References 1, 2 and 6) that critical power is a reasonably linear function of the inlet subcooling at constant mass flux and system pressure. [

]a,c A 10°C inlet subcooling corresponds to the reactor normal operating condition, and 44°C inlet subcooling covers the Loss of Feedwater Heating Anticipated Operational Occurrence.

4.2.4 Axial Power Distribution

Sub-bundle critical power data were obtained for a chopped cosine axial power distribution as well as for bottom-peaked and top-peaked axial power shapes. The cosine axial power shape is reasonably representative of typical operation. The bottom-peaked and top-peaked axial power shapes were selected to capture the effect of axial power shape over the range expected in reactor operation.

As discussed in Section 5, recent critical power measurements discussed in Reference 7 indicated that the Westinghouse boiling-length CPR correlations based on top-peaked, bottom-peaked, and cosine shaped axial power distributions may over-predict the assembly CPR for certain types of axial power distributions generally characterized as double-peaked shapes. The tests discussed in Reference 7 involved a single heated rod in a heated annulus conducted at the Royal Institute of Technology (KTH) in Stockholm, Sweden. Correction of the correlation to accommodate these test results is discussed in Section 5.

4.2.5 Local Power Distribution

The critical power performance of a test bundle is dependent on the test bundle local power distribution. One advantage of the FRIGG test loop is that the test bundle local power distribution can be easily varied. Systematic series of tests were conducted to investigate the critical power performance at various local peaking factors and various peak power rod locations. SVEA-96 Optima2 critical power measurements were obtained [ ]^{a,c} to establish the effect of local power distribution on critical power. Appendices B, C and D of this document show the nominal local power distributions tested. The local power distribution may differ slightly from point-to-point in tests with the same nominal radial power distribution, The local power distribution actually measured for each data point was used in the correlation development and evaluation.

The local power distributions used in the tests were designed to establish the local power distribution dependence of the bundle critical power performance. The local power distributions involve rods with peaking factors between [

]^{a,c}

The discussion of the range of individual parameters in Sections 4.2.1 through 4.2.5 can be summarized as follows. The ranges of parameters shown in Figures 4.1 through 4.4 were selected to cover values of parameters impacting Critical Power expected during normal BWR operations as well as Anticipated Operational Occurrences (AOOs) and relevant accidents. In selecting the test matrices, greatest emphasis is placed on those regions in which the reactor will usually operate. Therefore, while [

]^{a,c}

[

]a,c

4.2.6 Combinations of Parameters

In order to confirm that the parameter ranges considered in the Critical Power tests cover the combinations of conditions expected during typical reactor application, the parameter ranges expected during reactor operation are superimposed on the ranges of test points for combinations of parameters to which Critical Power is considered to be sensitive. As discussed in Section 5, [

]a,c

4.2.7 Summary

A side by side comparison of the range of the parameters in the tests with that of a typical reactor application is shown in Table 4.7. The combined range is based on the composite range of all the tests and is considered to be the range of validity of D4.1.1. As discussed in Section 4.2.6 and seen in Table 4.7, the range for a typical application is adequately bounded by the range of validity of D4.1.1.

Two methodologies for establishing CPR for a full assembly from [

]a,c. These methodologies were established to provide conservative full assembly CPR results for the applications for which they are used as discussed in Section 5.

4.3 DATA VALIDATION CRITERIA AND PROCEDURES

Data validation is supported with instrumentation performance reliability checks. All data collection instrumentation is periodically calibrated to assure the accuracy of the data.

The data validation process is further reinforced by assuring that all instrumentation is checked for proper operation prior to the performance of each test. Before and after each shift, a reading from every

transmitter is recorded and compared with the expected value for that transmitter. In the event of an abnormal reading, corrective actions are taken before the test is run. In addition, the following checks are performed at the beginning of each test period:

1. A heat balance is calculated to insure that power, flow, and temperature measurements are correct.

2. The overall pressure drops across the bundle at different flow rates are measured.

3. The sum of the power generated by each heater rod is compared with the sum of the power outputs from each power supply unit for all test points. These two bundle power measurements are accepted if they agree to within ±1%.

Critical power reference test points are periodically repeated to assure that the measurements are stable. The reference points for the SVEA-96 Optima2 test series are defined by the following nominal conditions:

[

]^{a,c}

The reproducibility of the critical power was found to be very good for the SVEA-96 Optima2 test series. Examples of the reproducibility are shown in Table 4.8. When the small differences in test parameters are accounted for, the reproducibility of the measured critical powers is excellent.

Conversion of the data to engineering units by the computer allowed preliminary test validation to be done upon completion of a run and before the data analysis took place. This preliminary validation provided immediate feedback on facility operation and data collecting equipment performance.

After the instrumentation had been functionally checked, and the test parameters and performance had been compared with the test matrix, the final data validation was performed during the data reduction and analysis stage.

4.4 DATA TRENDS

This section shows trends in the measured Critical Power data. These trends are addressed to confirm that the SVEA-96 Optima2 Critical Power database is physically realistic and consistent with similar measurements obtained for other assembly designs. The figures in this section show the measured data points and the corresponding D4.1.1 correlation predictions. The D4.1.1 CPR correlation is described in Section 5. The correlation predictions of critical power data are denoted with suffix "Pred". Furthermore, it should be noted that some spurious spread is introduced into the data when it is plotted in this manner

since all of the points were not obtained at precisely the target conditions for which the correlation was evaluated.

A test bundle is referred to with a designation such as SF24S. The designation SF24S (S=SVEA, F=FRIGG, 24 = number of rods, S = a serial number) stands for dryout power measurements on a SVEA-96 Optima2 sub-bundle test section with the cosine axial power shape. The designation SF24SB refers to dryout power measurements on a SVEA-96 Optima2 sub-bundle test section with the bottom-peaked axial power shape. The designation SF24ST refers to dryout power measurements on a SVEA-96 Optima2 sub-bundle test section with the top-peaked axial power shape.

The results from the cosine-peaked (SF24S), bottom-peaked (SF24SB) and top-peaked (SF24ST) tests at approximately [ ]^{a,c} are compared with correlation predictions for the uniform and optimized local power distributions, respectively, in Figures 4.9 and 4.10. "Uniform" local power distributions are intended to provide the same power to each of the 24 heater rods. The term "optimized" refers to a rod power distribution that gives the highest dryout power for a given set of mass flux, system pressure, inlet subcooling and axial power shape conditions. The optimized [

]^{a,c}

The critical power decreases as the axial power shapes become more top-peaked in Figures 4.9 through 4.10. This tendency is in agreement with measurements obtained for other assembly designs such as the SVEA-96 and SVEA-96+ design discussed in References 1 and 2. The monotonic increase in Critical Power as a function of mass flux is also consistent with other designs and the data obtained in other facilities. Therefore, the trends in these data reflect the expected dependence on assembly flow and axial power shape based on previous testing of earlier designs and the physical nature of the dryout process for various local power distributions.

Trends in exit pressure and inlet subcooling for various local power distributions are shown for the cosine-peaked axial power distribution (test bundle SF24S), bottom-peaked axial power distribution (test bundle SF24SB) and the top-peaked axial power distribution (test bundle SF24ST) in Figures 4.11 through 4.18, Figures 4.19 through 4.25, and Figures 4.26 through 4.32, respectively.

The influence of inlet subcooling at an exit pressure of approximately [

]^{a,c}

Critical power as a function of pressure for various constant mass flows and inlet subcooling are shown in Figures 4.13 to 4.18 for the cosine-peaked axial power shape in Figures 4.21 to 4.25 for the bottom-peaked axial power shape and Figures 4.28 to 4.32 for the top-peaked axial power shape. As shown in

these figures, [

]^{a,c} The same type of behavior as a function of system pressure was observed for the SVEA-96 and SVEA-96+ design reported in References 1 and 2 and is also consistent with other earlier designs.

The purpose of providing data trend plots in Figures 4.11 through 4.32 is to show that the trends in the data are physically reasonable and consistent with expectations. D4.1.1 predictions are included in these figures to help the correlation review as previously requested in the review of the ABBD1.0 and ABBD2.0 Correlations (References 1 and 2).

Table 4.1 Number of Points in SVEA-96 Optima2 Test Series

a,c

Table 4.2 Range of Test Parameters

a,c

Table 4.3 Number of Data Points in Various Parameter Ranges (All Three Axial Power Shapes) a,c

Table 4.4 Number of Data Points in Various Parameter Ranges (Cosine Axial Power Shapes) a,c

Table 4.5 Number of Data Points in Various Parameter Ranges (Bottom-Peaked Axial Power Shapes)

a,c

Table 4.6 Number of Data Points in Various Parameter Ranges (Top-Peaked Axial Power Shapes)

a,c

Table 4.7 Range of Parameters

a,c

[ ]

Table 4.8 Examples of Test Reproducibility

a,c

[ ]

a,c

Figure 4.1a Histogram for all SVEA-96 Optima2 Tests, Frequency Versus Mass Flux

a,c

Figure 4.2a Histogram from all SVEA-96 Optima2 Tests, Frequency Versus Pressure

a,c

Figure 4.3a Histogram from all SVEA-96 Optima2 Tests, Frequency Versus Subcooling

a,c

Figure 4.4a Histogram from all SVEA-96 Optima2 Tests, Frequency Versus R-factor

a,c

Figure 4.1b Histogram from SVEA-96 Optima2 Tests, Frequency Versus Mass Flux (Cosine Axial Power Shape)

a,c

Figure 4.2b Histogram from SVEA-96 Optima2 Tests, Frequency Versus Pressure (Cosine Axial Power Shape)

a,c

Figure 4.3b Histogram from SVEA-96 Optima2 Tests, Frequency Versus Subcooling (Cosine Axial Power Shape)

a,c

Figure 4.4b Histogram from SVEA-96 Optima2 Tests, Frequency Versus R-factor (Cosine Axial Power Shape)

a,c

Figure 4.1c Histogram from SVEA-96 Optima2 Tests, Frequency Versus Mass Flux (Bottom-Peaked Axial Power Shape)

a,c

Figure 4.2c Histogram from SVEA-96 Optima2 Tests, Frequency Versus Pressure (Bottom-Peaked Axial Power Shape)

a,c

Figure 4.3c Histogram from SVEA-96 Optima2 Tests, Frequency Versus Subcooling (Bottom-Peaked Axial Power Shape)

a,c

Figure 4.4c Histogram from SVEA-96 Optima2 Tests, Frequency Versus R-factor (Bottom-Peaked Axial Power Shape)

a,c

Figure 4.1d Histogram from SVEA-96 Optima2 Tests, Frequency Versus Mass Flux (Top-Peaked Axial Power Shape)

a,c

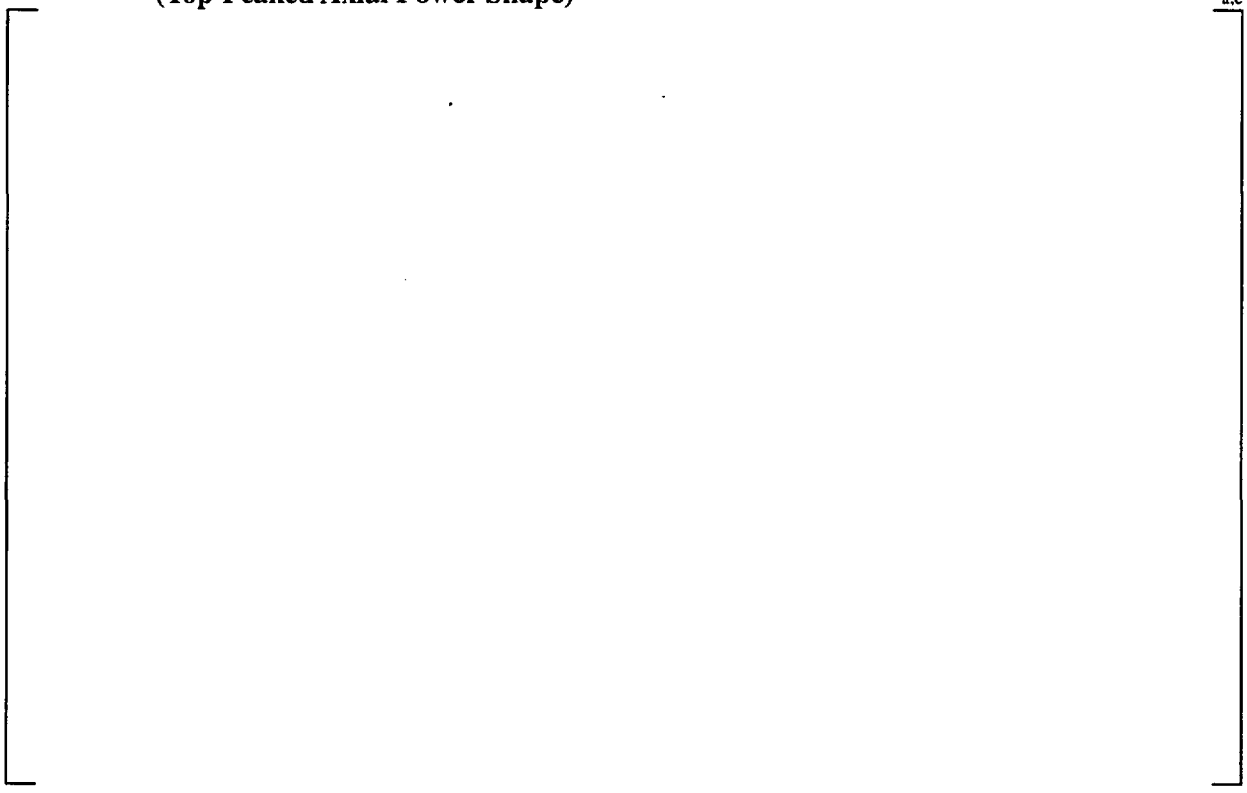

Figure 4.2d Histogram from SVEA-96 Optima2 Tests, Frequency Versus Pressure (Top-Peaked Axial Power Shape)

a,c

Figure 4.3d Histogram from SVEA-96 Optima2 Tests, Frequency Versus Subcooling (Top-Peaked Axial Power Shape)

a,c

Figure 4.4d Histogram from SVEA-96 Optima2 Tests, Frequency Versus R-factor (Top-Peaked Axial Power Shape)

Figure 4.5 Range of Test Parameters (Pressure vs. Mass Flux) Compared with Typical Application Range

a,c

Figure 4.6 Range of Test Parameters (Pressure vs. Subcooling) Compared with Typical Application Range

Figure 4.7 Range of Test Parameters (Subcooling vs. Mass Flux) Compared with Typical Application Range

a,c

Figure 4.8 Range of Test Parameters (R-factor vs. Mass Flux) Compared with Typical Application Range

a,c

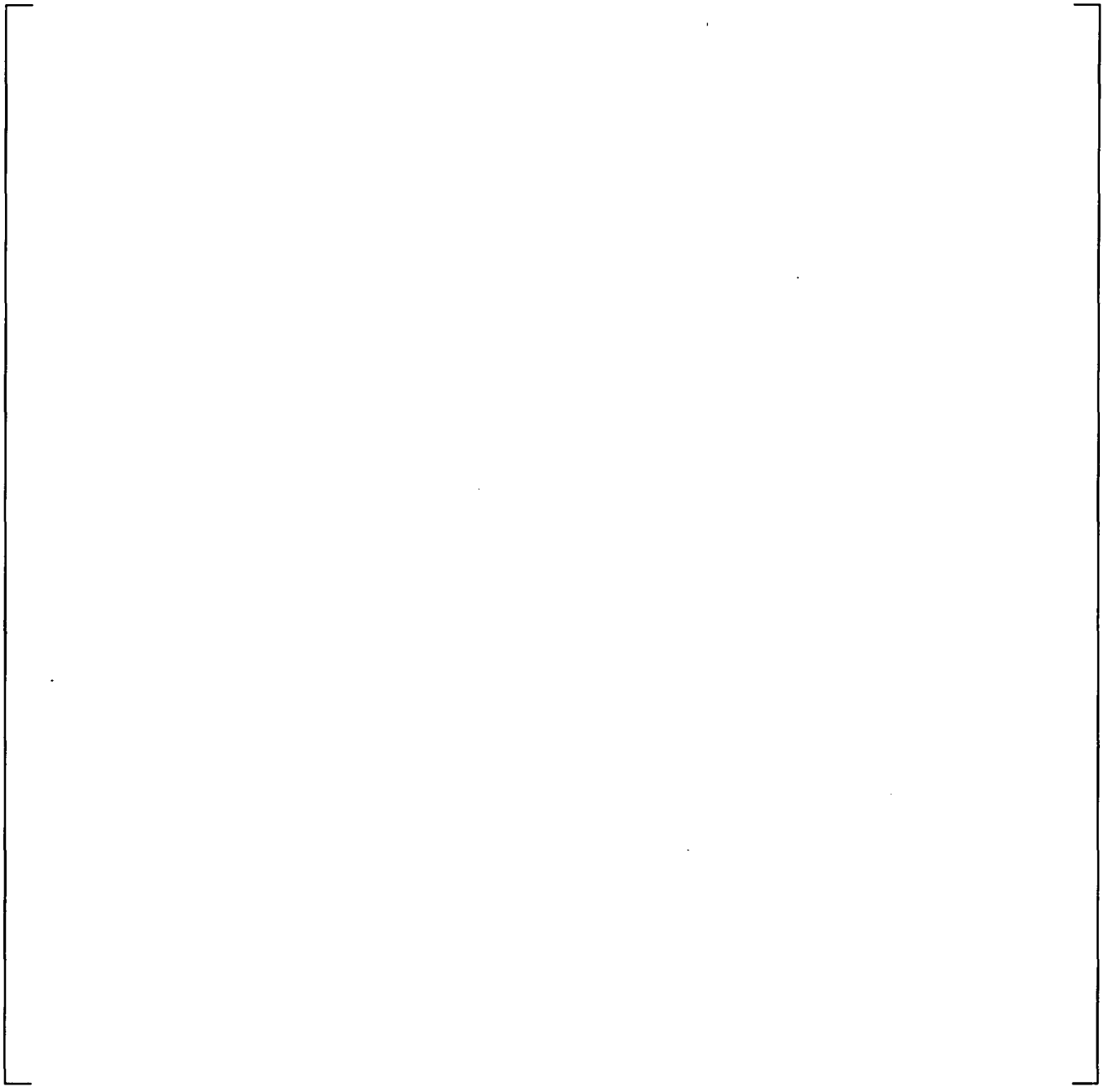

Figure 4.9 Critical Power Versus Flow at 70 Bar, 10 K Subcooling, for Uniform Local Power Distribution

a,c

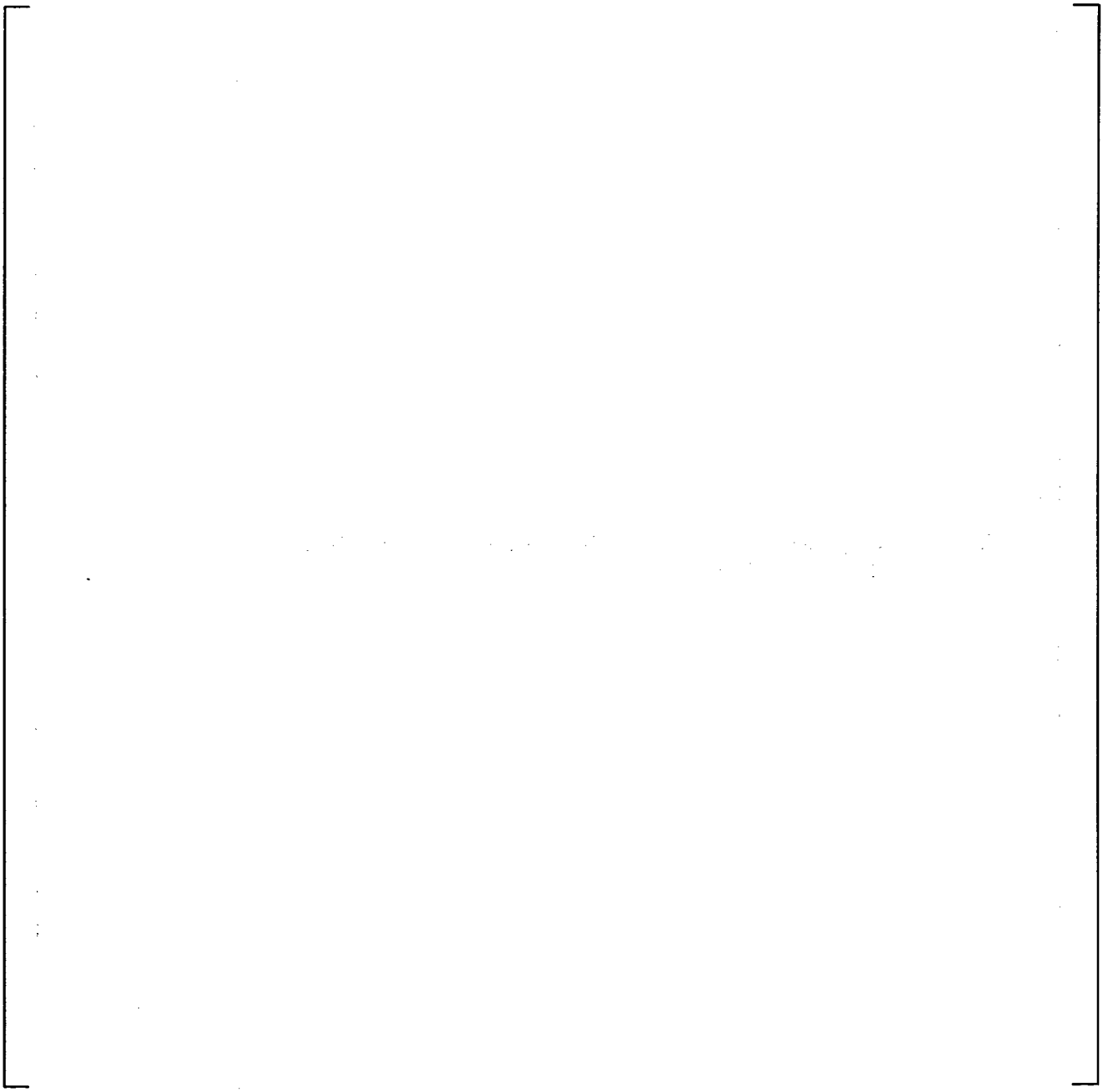

Figure 4.10 Critical Power Versus Flow at 70 Bar, 10 K Subcooling, for Optimized Local Power Distribution

a,c

Figure 4.11 SF24S Critical Power Versus Subcooling at 70 Bar, Uniform Local Power Distribution, for Various Flows

a,c

Figure 4.12 SF24S Critical Power Versus Subcooling at 70 Bar, Optimized Local Power Distribution, for Various Flows

a,c

Figure 4.13 SF24S Critical Power Versus Pressure at 10 K Subcooling, Uniform Local Power Distribution, for Various Flows

a,c

Figure 4.14 SF24S Critical Power Versus Pressure at 20 K Subcooling, Uniform Local Power Distribution, for Various Flows

a,c

Figure 4.15 SF24S Critical Power Versus Pressure at 30 K Subcooling, Uniform Local Power Distribution, for Various Flows

a,c

Figure 4.16 SF24S Critical Power Versus Pressure at 40 K Subcooling, Uniform Local Power Distribution, for Various Flows

a,c

Figure 4.17 SF24S Critical Power Versus Pressure at 10 K Subcooling, Optimized Local Power Distribution, for Various Flows

a,c

Figure 4.18 SF24S Critical Power Versus Pressure at 20 K Subcooling, Optimized Local Power Distribution, for Various Flows

Figure 4.19 SF24SB Critical Power Versus Subcooling at 70 bar, Uniform Local Power Distribution, for Various Flows

Figure 4.20 SF24SB Critical Power Versus Subcooling at 70 bar, Optimized Local Power Distribution, for Various Flows

a,c

Figure 4.21 SF24SB Critical Power Versus Pressure at 10 K Subcooling, Uniform Local Power Distribution, for Various Flows

a,c

Figure 4.22 SF24SB Critical Power Versus Pressure at 20 K Subcooling, Uniform Local Power Distribution, for Various Flows

a,c

Figure 4.23 SF24SB Critical Power Versus Pressure at 40 K Subcooling, Uniform Local Power Distribution, for Various Flows

a,c

Figure 4.24 SF24SB Critical Power Versus Pressure at 10 K Subcooling, Optimized Local Power Distribution, for Various Flows

a,c

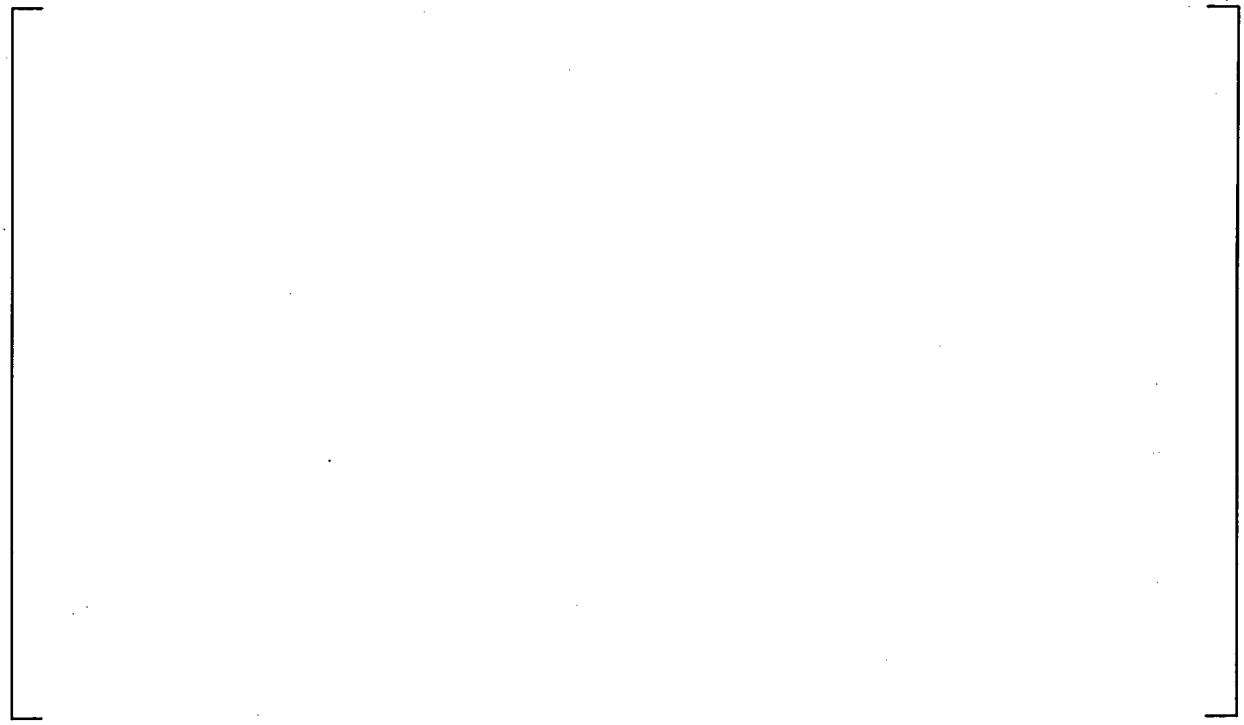

Figure 4.25 SF24SB Critical Power Versus Pressure at 20 K Subcooling, Optimized Local Power Distribution, for Various Flows

a,c

Figure 4.26 SF24ST Critical Power Versus Subcooling at 70 Bar, Uniform Local Power Distribution, for Various Flows

a,c

Figure 4.27 SF24ST Critical Power Versus Subcooling at 70 Bar, Optimized Local Power Distribution, for Various Flows

a,c

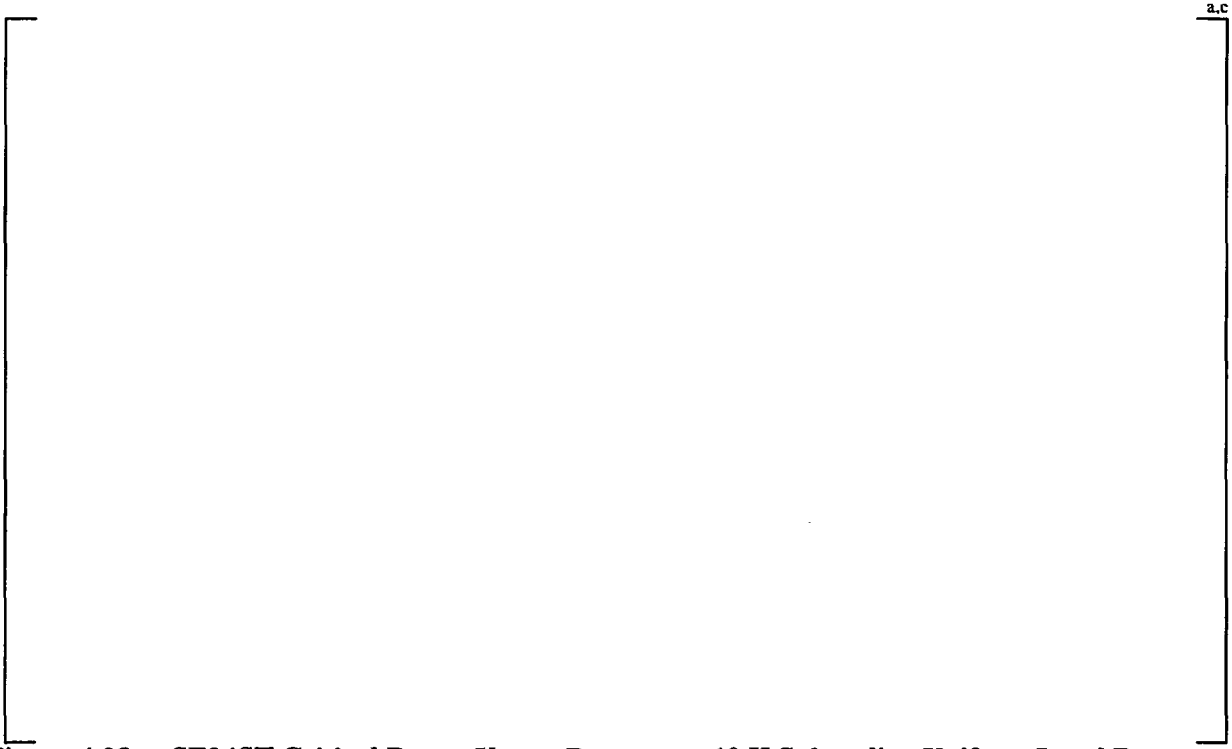

Figure 4.28 SF24ST Critical Power Versus Pressure at 10 K Subcooling Uniform Local Power Distribution, for Various Flows

a,c

Figure 4.29 SF24ST Critical Power Versus Pressure at 20 K Subcooling, Uniform Local Power Distribution, for Various Flows

a,c

Figure 4.30 SF24ST Critical Power Versus Pressure at 40 K Subcooling, Uniform Local Power Distribution, for Various Flows

a,c

Figure 4.31 SF24ST Critical Power Versus Pressure at 10 K Subcooling Optimized Local Power Distribution, for Various Flows

a,c

Figure 4.32 SF24ST Critical Power Versus Pressure at 20 K Subcooling, Optimized Local Power Distribution, for Various Flows

5 CRITICAL POWER CORRELATION

5.1 GENERAL D4.1.1 CORRELATION FORM

There are two common methods used to correlate critical power test data. One is to correlate the critical power test data in the critical quality-boiling length plane, and the other method is to correlate the critical power data in the critical heat flux-quality plane.

The critical quality-boiling length form has been selected to correlate the SVEA-96 Optima2 critical power test data.

Since the trends in the SVEA-96 Optima2 data are similar to trends for other BWR fuel, a critical quality-boiling length correlation would be expected to accurately correlate the SVEA-96 Optima2 data.

This decision is confirmed by the results in Section 6 which demonstrate that the critical quality-boiling length correlation described in this report sufficiently captures the dependence of all important parameters to which CPR is sensitive for the SVEA-96 Optima2 design. This SVEA-96 Optima2 critical power ratio correlation is described in this section and is referred to as the D4.1.1 correlation.

Experience has also shown that a critical quality-boiling length correlation represents a proven form capable of adequately predicting the onset of dryout during a transient. The process to confirm that D4.1.1 provides an adequate prediction of the change in critical power during a transient code application is described in Section 7.

The general trends in SVEA-96 Optima2 critical power as a function of system pressure, mass flux, and boiling length are qualitatively similar to trends in the data for the SVEA-96 and SVEA-96+ assemblies discussed in References 1 and 2. However, the quantitative behavior of SVEA-96 Optima2, SVEA-96 and SVEA-96+ is somewhat different. Therefore, while the same general type of CPR correlation is expected to be appropriate for various SVEA fuel designs, accurate prediction of SVEA-96 Optima2 CPR values requires coefficients and additive constants specific to the SVEA-96 Optima2 design. Additive constants specific to the SVEA-96 Optima2 assembly are required in the R-factor calculation to describe the dependence on SVEA-96 Optima2 critical power of different local power distributions.

Furthermore, the following improvements have been introduced in the D4.1.1 CPR correlation formulation relative to the ABBD1.0 and ABBD2.0 CPR correlations described in References 1 and 2:

1. [ ]^{a,c}

2. [ ]^{a,c}

3. [ ]^{a,c}

4. [
]^{a,c} and

5. [
]^{a,c}

These adaptations to the critical quality-boiling length correlation form with an [
]^{a,c} resulted in the D4.1.1 CPR correlation.

5.2 D4.1.1 CPR CORRELATION

Like the ABBD1.0 and ABBD2.0 correlations described in References 1 and 2, the D4.1.1 correlation is based on a critical quality-boiling length relationship. D4.1.1 correlates critical quality with [

]^{a,c}

The D4.1.1 correlation is a SVEA-96 Optima2 sub-bundle correlation in the sense that it is based on 24-rod sub-bundle data. Calculation of sub-bundle CPR is discussed in this section. Application of the D4.1.1 correlation to a full SVEA-96 Optima2 assembly is discussed in Section 5.4.

All parameters discussed below are in SI units unless otherwise noted.

The correlation terms in the D4.1.1 CPR correlation are best-fit functions that describe the critical steam quality dependence on [ ]^{a,c} on the test data. Correlation coefficients were systematically optimized by minimizing the critical steam quality error as a function of [ ]^{a,c}. Additive constants to the R-factor were established which [
]^{a,c} observed in the test data.

5.2.1 Correlation

The D4.1.1 critical power ratio is defined as:

[ ]^{a,c} Equation 5.2-1

where:

[

]^{a,c}

[

]^{a,c}

where

[

]^{a,c}

Q_{real} = the actual sub-bundle power

[ ]^{a,c} Q_c is defined by the following iteration process:

[ ]^{a,c}

where:

ε = iteration limit

[

]^{a,c}

where

[ ]^{a,c}

The correlation terms derived in this way are as follows:

[

]^{a,c}

where

[

]^{a,c}

where

[

]^{a,c}

where

[

]^{a,c}

where

[

]^{a,c}

where

[

]^{a,c}

The limitations to the AN parameter are defined as follows:

[

]^{a,c}

where

[

]^{a,c}

The application of these limitations on [

]^{a,c}

where

[

]^{a,c}

where

[

]^{a,c}

where

[

]^{a,c}

The boiling length (BL) is calculated as the distance from the starting point of bulk boiling (Blen) [

]^{a,c}

The [

]^{a,c}

The [

]^{a,c}

where

[

]^{a,c}

Each of the correlation terms is shown in graphical form as a function of its normalized parameter in Figures 5.1 through 5.3. In each case the subscript in the correlation function is referred to as a capital letter to facilitate reading the legends in the graphs [

]^{a,c} The range over which the D4.1.1 correlation is valid is provided in Section 6.

5.2.2 Sub-bundle R-factor for SVEA-96 Optima2

The R-factor accounts for the local power distribution (relative rod power distribution in the sub-bundle), cross section geometry, and the spacer grid configuration.

[

]^{a,c}

where

[

]^{a,c}

S = number of active rods in a given axial zone. [

]^{a,c}

Referring to the rod index definitions in Figure 5.4, the weighting factors are defined as follows:

[

]^{a,c}

[

]^{a,c}

The relative rod power distributions at a [
]^{a,c}.

[ ]^{a,c}

where

[

]^{a,c}

For nodes, z, above the [

]^{a,c}.

Inhomogeneous features of the sub-bundle design which are not captured by the linear combinations of the [

]^{a,c} as shown in Figure 5.5.

[

]^{a,c}

The R-factor, [

]^{a,c} Equation 5.2.2-1

where

[

]^{a,c}

Then the value of [

]^{a,c}

where

"node" = number of active nodes

The resulting [ ]^{a,c} is shown in the following figure:

a,c

[

]

5.2.3 Determination of D4.1.1 Additive Constants

As shown in Table 4.1, the SVEA-96 Optima2 data base is extensive. Therefore, a systematic approach was required to establish the additive constants and correlation coefficients:

1. The SVEA-96 Optima2 additive constants in Figure 5.5 were established from [

   ]^{a,c}

2. This selection was performed for a [

   ]^{a,c}

   It should be noted that the principles used to develop the additive constants for D4.1.1 are the same as those used to establish the additive constants for ABBD1.0 and ABBD2.0 described in References 1 and 2. Detailed descriptions of the development of additive constants and the associated uncertainties were presented in the responses to Request Numbers 13 and 34 in Reference 2.

   The SVEA-96 Optima2 local power data base was selected to include local power distributions for which the [

   ]^{a,c}

3. Using the additive constants established in Step 1, the [

   ]^{a,c}

   The division of the [

   ]^{a,c}

[

]a,c

The sorting procedure was performed [
]a,c

With the R-factor [

]a,c

4. The resulting D4.1.1 CPR correlation was validated relative to the validation data set as described in Section 6 and relative to the transient data as described in Section 7.

5.3 DOUBLE PEAK CORRECTION

The D4.1.1 CPR correlation is based on top-peaked, bottom-peaked, and cosine-shaped axial power distributions. As shown in Section 6, this correlation exhibits a very good fit to the 1819-point FRIGG Loop database described in Section 4. [

]a,c Current BWR industry practice is to base critical power tests on these three axial power shapes, and this assumption has generally proven to be appropriate. However, the recent KTH test data; such as that shown in Reference 7, indicates that boiling length CPR correlations, including the D4.1.1 correlation, may over-predict CPR for double-peaked axial power shapes.

The possibility that the Westinghouse boiling length CPR correlations may over-predict the assembly CPR for double-peaked axial power shapes is based on critical power measurements for a single heated rod in a heated annulus conducted recently at the Royal Institute of Technology (KTH) in Stockholm, Sweden. A description of some of these KTH measurements is provided in Reference 7. The tests described in Reference 7 involved an annular geometry consisting of one heated central test rod within a concentric heated outer tube. The benefit of this relatively simple KTH geometry is that it facilitates testing of a relatively broad spectrum of axial power shapes. [

]a,c

While the KTH geometry is not entirely representative of the Westinghouse SVEA 10x10 geometric configurations including the SVEA-96 Optima2 assembly, the possibility exists that the non-conservative trends implied by the tube data could occur for Westinghouse 10x10 SVEA fuel design critical quality-boiling length CPR correlations, including the D4.1.1 correlation. [

]^{a,c} The correction factor is [

]^{a,c} when applied [ ]^{a,c} to the CPR predicted by the critical quality-boiling length correlation such as D4.1.1.

The correction factor is established through the following two-step process:

[

]^{a,c}

Specifically the correction factor is given by:

[

]^{a,c}

Figure 5.7 illustrates the establishment of the correction factor. Assuming that Node 1 is the bottom of the assembly, [

]^{a,c}

Derivation of the correction factor in this manner [

]^{a,c}

As discussed in Reference 3, Westinghouse intends to use the correction factor described in this section for licensing analyses with SVEA-96 and SVEA-96+ assemblies currently operating in the U.S. Reference 3 is currently under review at the NRC.

5.4 APPLICATION OF D4.1.1 CORRELATION TO FULL SVEA-96 OPTIMA2 ASSEMBLY

A special consideration in calculating the R-factor for the SVEA-type assemblies has to do with the fact that the SVEA channel consists of four sub-channels separated by a water cross with flow communication slots between the sub-channels along the channel length. Each sub-channel contains a sub-bundle.

CPR correlations for SVEA-type assemblies, such as D4.1.1 and ABBD1.0 and ABBD2.0 described in References 1 and 2, respectively, are based on 24-rod sub-bundle data. Since the CPR correlation is applied to full (e.g., 96-rod) SVEA-type assemblies in design and licensing applications as well as for CPR monitoring in the plant Core Monitoring System, the impact on critical power caused by a mismatch in the power between the sub-bundles and the flow mismatch caused by this power mismatch must be taken into account. [

]^{a,c} As described in References 1, 2, and 3, this power mismatch in SVEA-type fuel has been accounted for in the past in Westinghouse boiling-length critical-quality CPR correlations by an adjustment to the [ ]^{a,c} CPR calculation by a factor referred to as the "Mismatch Factor." As discussed in Section 5.4.1 for D4.1.1, and References 1 through 3 for SVEA-96 and SVEA-96+, the Mismatch Factor is derived by [

]^{a,c} The Mismatch Factor for D4.1.1 is discussed in Section 5.4.1.

Treatment of the sub-channel power mismatch [

]^{a,c} This approach is referred to as the Sub-bundle Model and is described for D4.1.1 in Section 5.4.2.

The Sub-bundle Model described in Section 5.4.2 will augment the Mismatch Factor method discussed in Section 5.4.1 in a manner which assures that the D4.1.1 CPR correlation does not over-predict margins to dryout. [

]^{a,c}

5.4.1 Mismatch Factor Method

As discussed above, the Mismatch Factor Method involves [

]^{a,c}.

The Mismatch Factor Method to account for power mismatch in sub-bundles is based on [

]^{a,c}

Utilizing the change in critical power [

]^{a,c}

The D4.1.1 mismatch factor defined by equation 5.4.1-1 is plotted in Figure 5.6.

Since the mismatch factor is intended to capture the flow mismatch associated with power mismatch, and the [

]^{a,c}

5.4.2 Sub-bundle Model

[

]^{a,c}

[ ]^{a,c} our understanding is that most current core simulators supporting on-line Core Monitoring Systems only have the capability to calculate converged power/void distributions on a full assembly basis.

Accordingly, Westinghouse has developed a simplified method of accommodating sub-bundle power mismatch in SVEA-type fuel [ ]^{a,c}. This improved method is referred to as the "Sub-bundle Model" and is described in this Section. This Sub-bundle Model approach of calculating the CPR [ ]^{a,c} represents a substantial improvement for establishing SVEA assembly steady-state CPR relative to the Mismatch Factor method described in Section 5.4.1. The Mismatch Factor approach described above also [

]^{a,c}

The Sub-bundle Model [

]^{a,c}

1. [

]^{a,c}

2. [

]^{a,c}

3. [

]^{a,c}

4. [

]^{a,c}

[

]^{a,c}

5.4.3 Conservative Assembly CPR Based on Sub-bundle CPR

The lateral flow communication channels between the SVEA sub-bundles are [

]^{a,c}

The sub-channel power mismatch associated with sub-channel power mismatch represents a deterministic, physical effect. [

]^{a,c}

[

]^{a,c}

This effect is accommodated by the multiplicative factor, [

]^{a,c}

In summary, [

]^{a,c} The mean D4.1.1 correlation error and standard deviation reflecting the correlation fit to the FRIGG Loop data is discussed in Section 6.

a,c

Figure 5.1 The X_G, X_B, X_P and X_A Functions

a,c

Figure 5.2 The $X_{G,P}$, $X_{G,B}$, $X_{P,A}$, $X_{B,A}$, and $X_{A,G}$ Functions

Figure 5.3 The Linear Term and Cross Term in CFR Defined in Section 5.2.1 (i.e., f(RN) = -82.9 · 10^{-3} · RN and f(RN*GN) = -0.75 · 10^{-3} · RN · GN)

Figure 5.4 Rod Index

Figure 5.5 SVEA-96 Optima2 Additive Constants

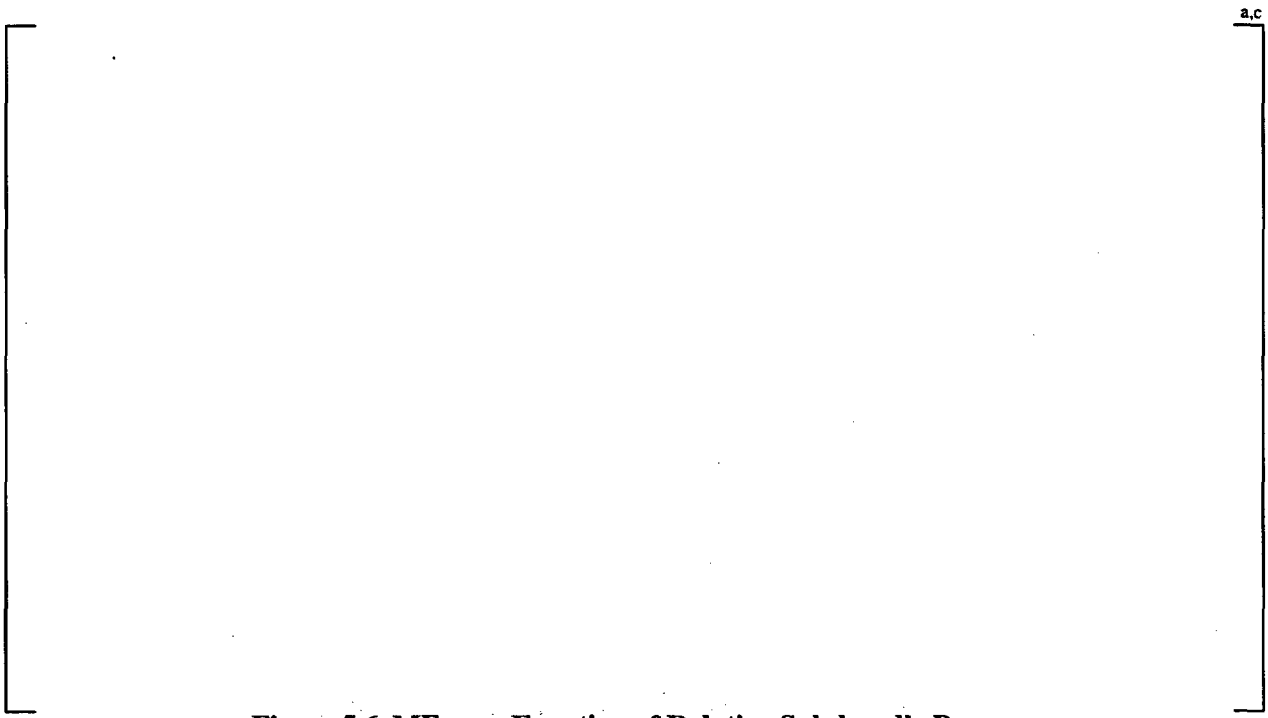

Figure 5.6 MF_s as a Function of Relative Sub-bundle Power

a,c

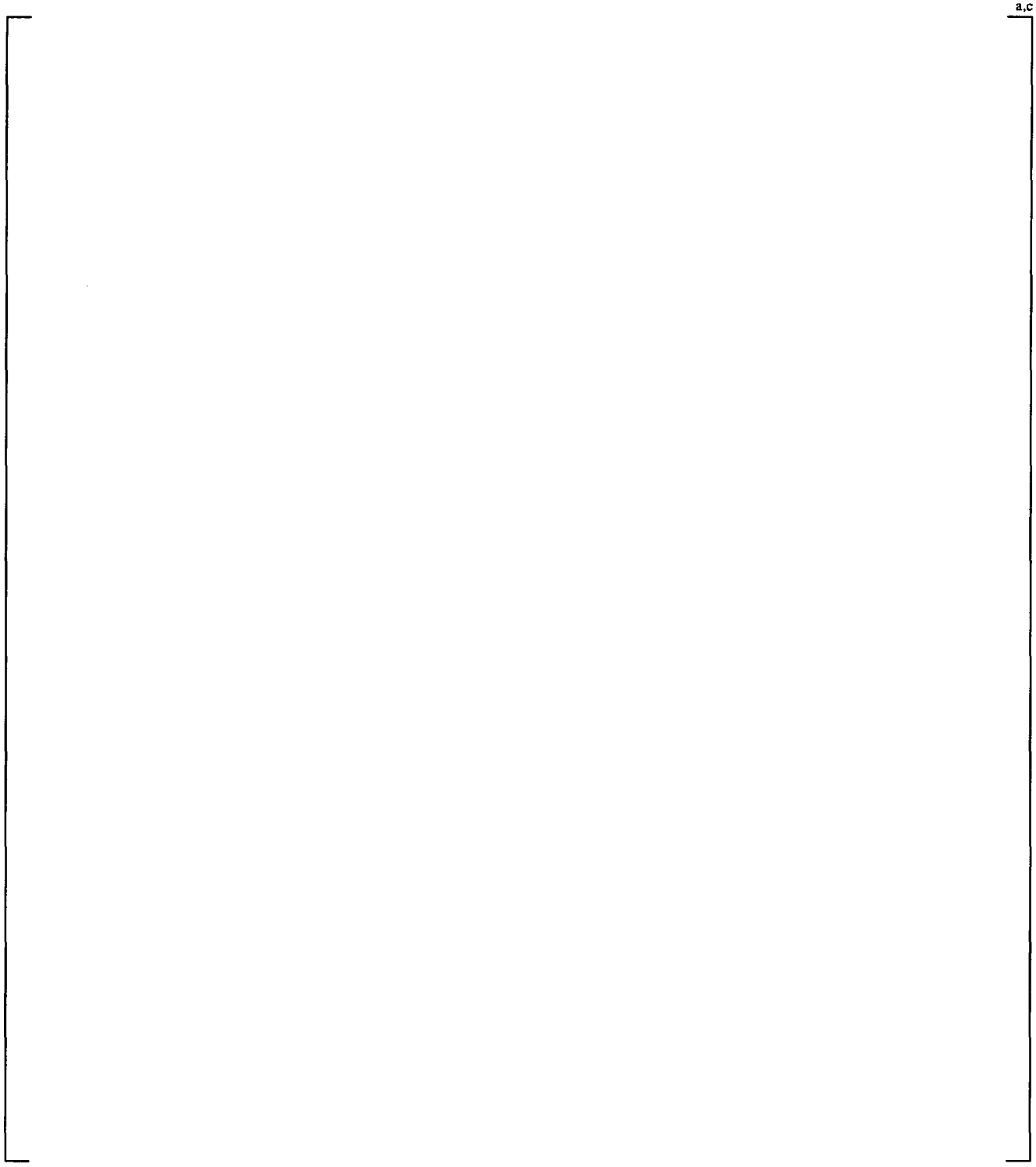

Figure 5.7 Example of Axial Shapes Defining Correction Factor

6 CORRELATION EVALUATION

The functional form of the D4.1.1 dryout correlation has been developed to correlate the critical power test data in the critical quality-boiling length plane.

The D4.1.1 CPR correlation data base is composed of a total of [ ]^{a,c} steady state critical power measurements. Evaluation of the D4.1.1 CPR correlation relative to the steady state data base is contained in this section. In addition, Section 7 contains the evaluation of the D4.1.1 CPR correlation relative to transient critical power measurements.

The steady state CPR data base is composed of [ ]^{a,c} points measured with a full scale 24-rod sub-bundle. This critical power data base was divided into two data sets. The [ ]^{a,c} evaluation data set represented 80% of the data base and was used in the correlation derivation. The [ ]^{a,c} validation data set represents 20% of the data base and was used for validation of the D4.1.1 CPR correlation. The number of data points and local power distributions for the evaluation and validation data sets are summarized in Tables 6.1 and 6.2, respectively.

The 24-rod SVEA-96 Optima2 data base obtained with the cosine, bottom and top-peaked axial power distribution and test bundle local power distributions used to generate that data base are shown in Appendix B, C and D respectively.

6.1 D4.1.1 PERFORMANCE RELATIVE TO THE SVEA-96 DATA BASE

Table 6.3 shows mean prediction errors, standard deviations, numbers of data points, and 95/95 tolerance limits for the D4.1.1 CPR correlation relative to the entire 24-rod SVEA-96 Optima2 data base as well as relative to subsets of that data base. The prediction error, ε, is given by:

$$\varepsilon = \left[\frac{\text{predictedpower}}{\text{measuredpower}} - 1\right] \times 100 \qquad \text{Equation 6-1}$$

As shown in Table 6.3, the mean prediction error and standard deviation over the entire SVEA-96 Optima2 data base is [ ]^{a,c}, respectively. The mean prediction error and standard deviation [ ]^{a,c}. Since the validation data set was selected in a systematic, unbiased manner over the entire data base, [ ]^{a,c}.

A useful graphical validation technique for a calculated function is to plot the function versus the measured values. Figure 6.1 is a comparison of the critical powers predicted with the D4.1.1 correlation as a function of the measured critical powers for all [ ]^{a,c} data points used to develop and validate the correlation. The solid lines in Figure 6.1 represent variations from the correlation prediction of ± 5%. The designations "C," "B," and "T" refer to data obtained with chopped cosine, bottom-peaked, and top-peaked axial power distributions, respectively. As shown in Figure 6.1, the D4.1.1 correlation shows

good agreement with the measured data and does not show a bias as a function of critical power. Table 6.4 provides the number and percentage of predictions exceeding the 5% boundary.

Another standard graphical validation technique is to plot the prediction error, ε, versus parameters to which the function is sensitive. An ideal prediction is characterized by ε = 0.0. Accordingly, the prediction error is plotted as a function of [

]^{a,c} in Figures 6.2 through 6.8. The prediction error, ε, is defined by Equation 6-1.

Figure 6.2 is a plot of the prediction error for the D4.1.1 correlation relative to the entire [

]^{a,c}

Figure 6.4 is a plot of the prediction error for the D4.1.1 correlation relative to the entire [

]^{a,c}

Figure 6.5 is a plot of the prediction error for the D4.1.1 correlation relative to the [

]^{a,c}

Figures 6.6 and 6.7 are plots of the prediction error for the D4.1.1 correlation relative to the [

]^{a,c}

Figure 6.8 is a plot of the prediction error for the D4.1.1 correlation relative to the [

]^{a,c}

In Summary, Figures 6.2 through 6.8 demonstrate that the D4.1.1 correlation provides a good fit to the test data with no systematic biases which would limit the validity of the correlation to predict the bundle critical power performance in design and licensing applications.

Figure 6.9 is a frequency distribution of the prediction error for the SVEA-96 Optima2 data base. [

]^{a,c}

[

]^{a,c}

Figure 6.10 shows the critical power dependence on axial power shape and mass flux predicted by D4.1.1. Note that the intent of Figure 6.10 is to show the trends for various axial power shapes. A nominal condition is assumed for these correlation predictions. There are no measured data at these precise conditions for direct comparison. As shown in Figure 6.10, [

]^{a,c}

Similarly, Figure 6.11 shows the D4.1.1 critical power dependence on inlet subcooling for several different mass flux values. As shown in Figure 6.11, [

]^{a,c}

Table 6.5 shows the mean prediction error and standard deviation in the mean prediction error, the number of data points, and the 95/95 tolerance limits [

]^{a,c}

Figures 6.12 through 6.14 presents the same information as Figure 6.2 in which the Prediction Errors are plotted as a function of mass flux for the cosine-shaped, bottom-peaked, and top-peaked axial power shapes, respectively. Table 6.6 provides the mean prediction errors, standard deviations and numbers of data points for the various mass flux ranges.

Additional plots of the prediction error as a function of mass flux, pressure, and inlet subcooling for selected subsets of the data base including the fringe areas of operation are presented in Figures 6.15 through 6.32. As can be seen from these figures, there are no significant trends or biases in the D4.1.1 correlation. These figures demonstrate that the D4.1.1 CPR correlation is applicable in the fringe areas of operation, and is supported by a sufficient number of data points in these areas. The figures also illustrate the good performance of the correlation at nominal conditions.

In summary, the following conclusions can be drawn from comparison of the D4.1.1 correlation predictions with the 24-rod SVEA-96 Optima2 data base:

1. All trends in the critical power data base discussed in Section 4 are adequately captured with the D4.1.1 CPR correlation. Furthermore, predicted critical power trends with [ ]^{a,c} are consistent with previous dryout testing of earlier assembly designs.

2. The quality of the predictions of the D4.1.1 CPR correlation does not show any evidence [

]^{a,c}

3. Therefore, it is concluded that the D4.1.1 CPR correlation provides a satisfactory fit to the data to justify its use for design and licensing applications. A normal uncertainty distribution with a mean error of [ ]^{a,c} provides a good characterization of the prediction error distribution for the SVEA-96 Optima2 data base.

6.2 CORRELATION UNCERTAINTY AND RANGE OF THE CORRELATION

Based on the evaluations in Section 6.1, it is concluded that the best estimate of the D4.1.1 CPR correlation mean prediction error and standard deviation in the mean prediction error should be based on the [

]^{a,c} will be used for design and licensing applications. A detailed description of the treatment of the correlation uncertainty in a design and licensing application is provided in Reference 2 (see ABB response to NRC Request Number 13).

The range over which the D4.1.1 CPR correlation is valid is shown in Table 6.7. This range is based on the entire [

]^{a,c}

Table 6.1 Number of Data Points and Local Power Distributions (Evaluation Data Set)

a,c

Table 6.2 Number of Data Points and Local Power Distributions (Validation Data Set)

a,c

Table 6.3 Mean Prediction Errors and Standard Deviations for D4.1.1 CPR Correlation

a,c

Note:
1. Prediction Error is defined by Equation 6-1

Table 6.4 Number and Percent of Calculated Data Points Exceeding the 5% Boundary

a,c

Table 6.5 Mean Prediction Error and Standard Deviations for D4.1.1 CPR Correlation for Data Ranges

a,c

Note: Range a to b means $a \leq x < b$

Table 6.6 Mean and Standard Deviations in Mean Prediction Error for Various Mass Flux Ranges

a,c

Note: Range is defined as Lower Bound < Mass Flux ≤ Upper Bound

Table 6.7 Range of Validity of D4.1.1

a,c

Figure 6.1 D4.1.1 Predicted Versus Measured Critical Power for all Data Points – the Lines Represent ±5% Error

Figure 6.2 D4.1.1 Prediction Error as a Function of Mass Flux for all Data Points

a,c

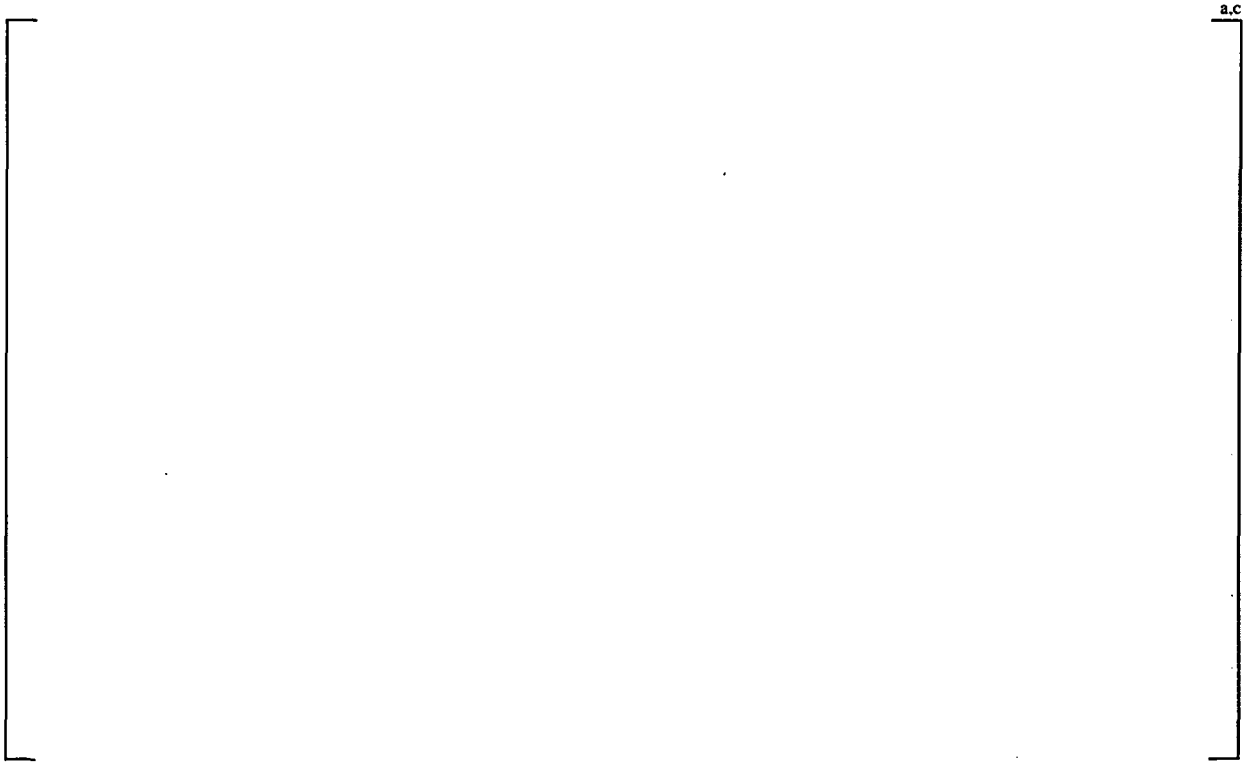

Figure 6.3 D4.1.1 Prediction Error as a Function of Mass Flux for Validation Data

a,c

Figure 6.4 D4.1.1 Prediction Error as a Function of Outlet Pressure for all Data Points

a,c

Figure 6.5 D4.1.1 Prediction Error as a Function of Inlet Subcooling for all Data Points

a,c

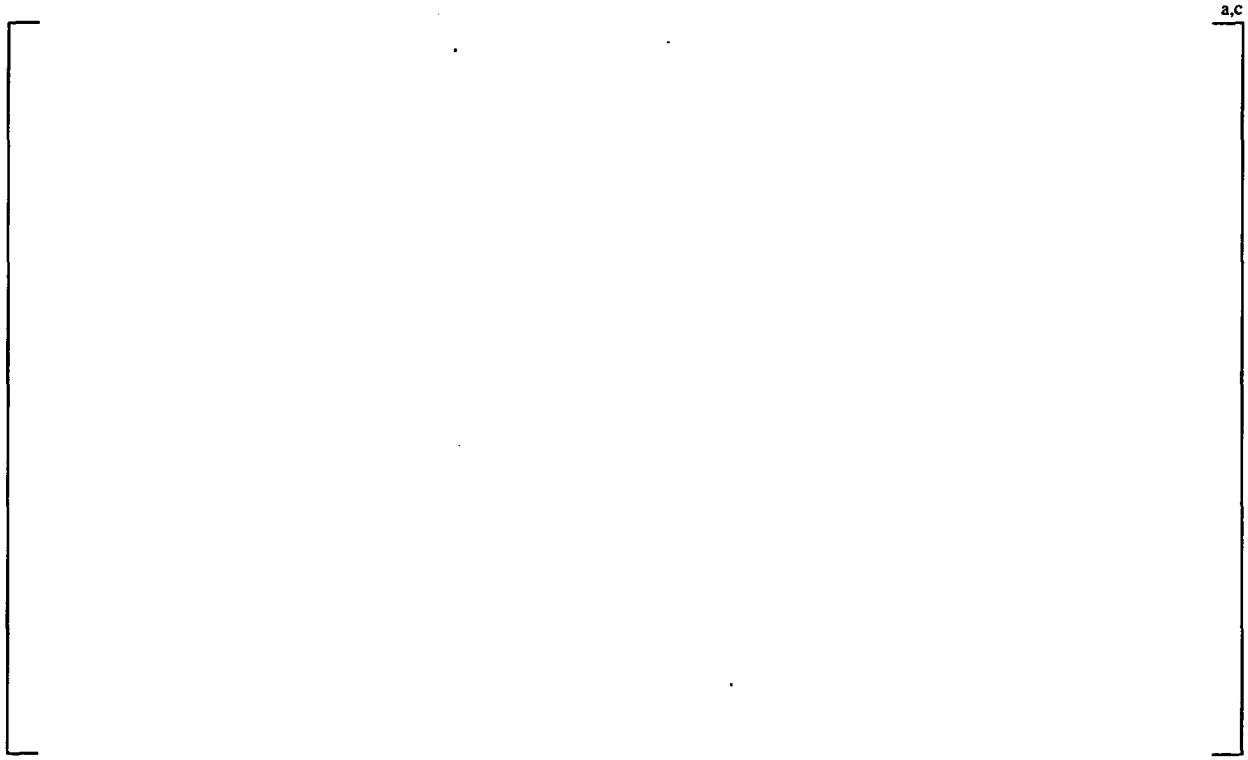

Figure 6.6 D4.1.1 Prediction Error as a Function of Boiling Length for all Data Points

a,c

Figure 6.7 D4.1.1 Prediction Error as a Function of Annular Flow Length for all Data Points

a,c

Figure 6.8 D4.1.1 Prediction Error as a Function of R-factor for all Data Points

a,c

Figure 6.9 D4.1.1 for all Test Data – Histogram of Frequency Versus CPR Error

a,c

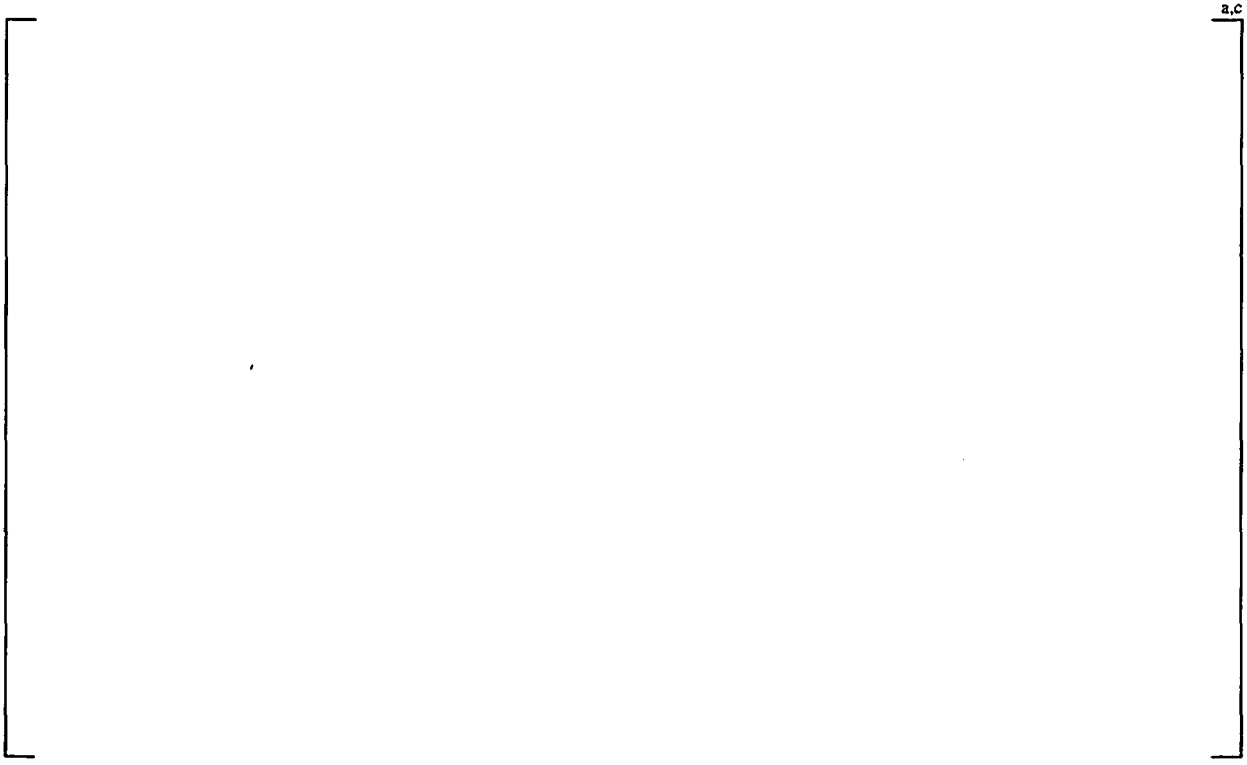

Figure 6.10 D4.1.1 Critical Power Dependence on Axial Power Shape (Pressure = 70 bar, Subcooling = 10K, R-factor = 0.93)

a,c

Figure 6.11 D4.1.1 Critical Power Dependence on Subcooling

a,c

Figure 6.12 Mean Prediction Error as a Function of Mass Flux – Cosine Axial Power Profile

a,c

Figure 6.13 Mean Prediction Error as a Function of Mass Flux – Bottom-Peaked Axial Power Profile

a,c

Figure 6.14 Mean Prediction Error as a Function of Mass Flux – Top-Peaked Axial Power Profile

a,c

Figure 6.15 Prediction Error Versus Mass Flux at 35 Bar

a,c

Figure 6.16 Prediction Error Versus Mass Flux at 70 Bar

a,c

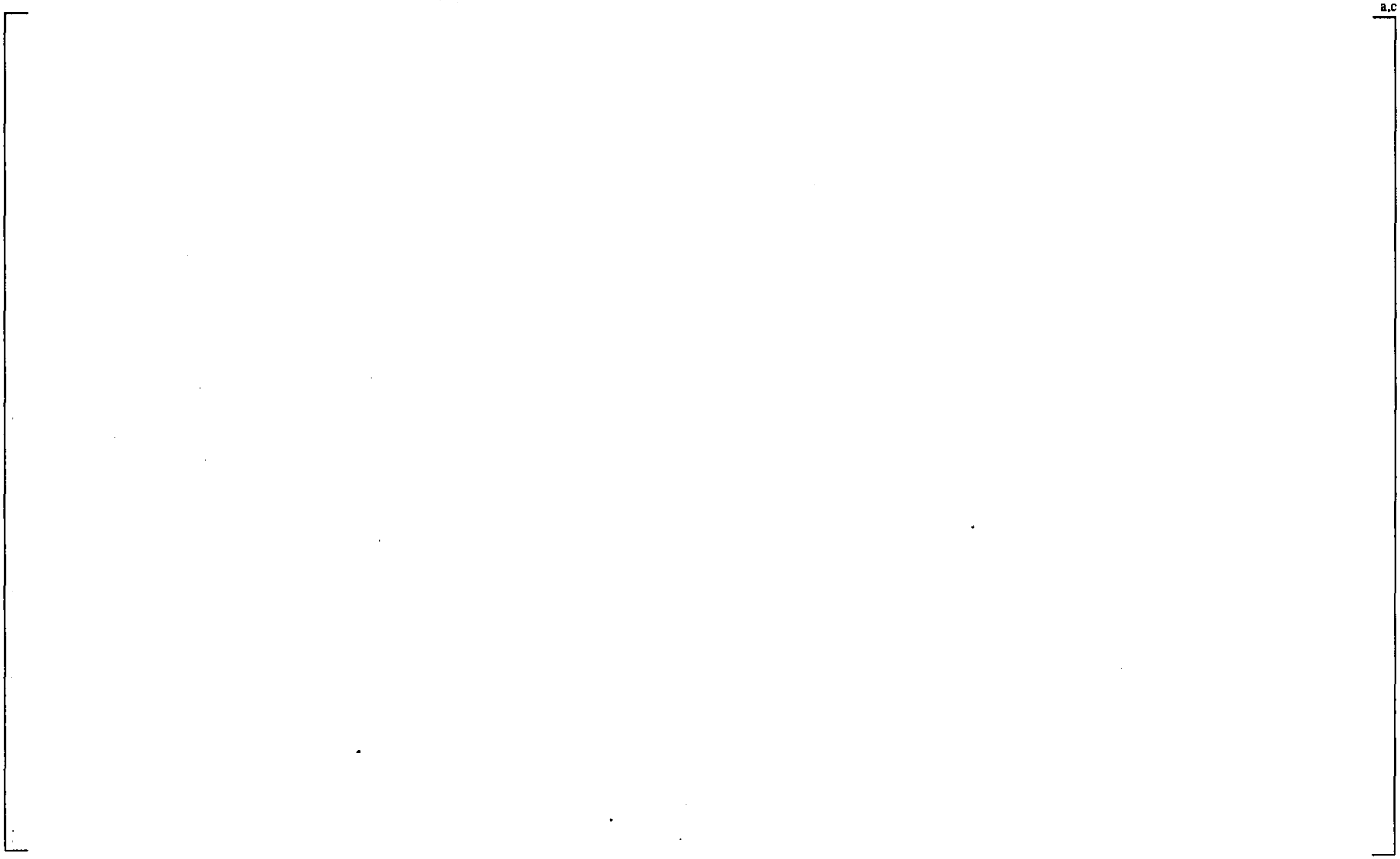

Figure 6.17 Prediction Error Versus Mass Flux at 80 Bar

a,c

Figure 6.18 Prediction Error Versus Subcooling at 35 Bar

a,c

Figure 6.19 Prediction Error Versus Subcooling at 70 Bar

a,c

Figure 6.20 Prediction Error Versus Subcooling at 80 Bar

a,c

Figure 6.21 Prediction Error Versus Mass Flux at 10 Degree C Subcooling

a,c

Figure 6.22 Prediction Error Versus Mass Flux at 20 Degree C Subcooling

a,c

Figure 6.23 Prediction Error Versus Mass Flux at 40 Degree C Subcooling

a,c

Figure 6.24 Prediction Error Versus Mass Flux for an R-factor of 0.91

a,c

Figure 6.25 Prediction Error Versus Mass Flux for an R-factor of 0.93

a,c

Figure 6.26 Prediction Error Versus Mass Flux for an R-factor of 0.95

a,c

Figure 6.27 Prediction Error Versus Pressure for an R-factor of 0.91

a,c

Figure 6.28 Prediction Error Versus Pressure for an R-factor of 0.93

a,c

Figure 6.29 Prediction Error Versus Pressure for an R-factor of 0.95

a,c

Figure 6.30 Prediction Error Versus Subcooling for an R-factor of 0.91

a,c

Figure 6.31 Prediction Error Versus Subcooling for an R-factor of 0.93

a,c

Figure 6.32 Prediction Error Versus Subcooling for an R-factor of 0.95

7 CONFIRMATION FOR TRANSIENT APPLICATION

7.1 INTRODUCTION

One specified acceptable fuel design limit (SAFDL) is that no more than 0.1% of the fuel rods in the core experience boiling transition under normal operation and anticipated operational occurrences (AOOs). This requirement is typically satisfied by evaluating the change in CPR (ΔCPR) during licensing basis AOOs and establishing a CPR operating limit such that the SLMCPR will not be violated during limiting transient events.

Transient CPR predictions involve evaluation of the flow, enthalpy, and pressure in the fuel assembly at each axial node as a function of time during the transient. A transient systems analysis code is used to calculate the transient fluid parameters. These parameters are then used with the steady-state CPR correlation for an assembly to evaluate transient CPR. One transient systems analysis code used by Westinghouse for CPR predictions is the BISON-SLAVE channel model of the BISON transient analysis code documented in References 4 and 5.

The methodology for demonstrating that the application of the D4.1.1 correlation in transient calculations will provide conservative predictions of ΔCPR is described in this section. Specifically, the process for qualifying implementation of the D4.1.1 correlation in transient codes is described. Then, the transient experiments performed in the FRIGG test loop to qualify the transient code implementation for SVEA-96 Optima2 are described. Finally, the D4.1.1 correlation validation in the BISON-SLAVE transient code is presented.

7.2 TRANSIENT IMPLEMENTATION VALIDATION METHODOLOGY

The two objectives of the transient systems analysis code implementation validation are to:

1. Confirm proper implementation of the steady-state CPR correlation in the transient code, and

2. Confirm the capability of the steady-state CPR correlation implemented in the transient code to calculate dryout during transients with adequate accuracy to provide conservative predictions of ΔCPR.

Transient code implementation of the D4.1.1 CPR correlation is validated for each code application by
[

]^{a,c}

[

]^{a,c}

7.3 TRANSIENT DRYOUT EXPERIMENTS

The transient tests used to validate the D4.1.1 correlation resulted in a transient validation data base for the Westinghouse SVEA-96 Optima2 fuel design. The transient CPR data were taken in controlled transient experiments performed in the FRIGG test loop. The measurements were performed for three different axial power profiles and included numerous different initial parameter variations as well as transient event simulations. The application of these tests to validate the D4.1.1 correlation for transient applications is described in this section.

7.3.1 FRIGG Loop

The transient tests for SVEA-96 Optima2 were carried out with the test bundles described in Section 3 incorporating the three axial power profiles:

- Bottom-peaked using Test bundle SF24SB
- Cosine-shaped using Test bundle SF24S
- Top-peaked using Test bundle SF24ST

Therefore, the transient tests were performed with the same test sections and test facility used in the steady-state experiments described in Section 3, and the three axial power distributions used in the transient tests are shown in Figure 3.4. Both power increase transients and flow reduction transients are simulated in the FRIGG loop transient tests. [

]^{a,c}

A power supply controller capable of producing power pulses providing heat flux variations which simulate BWR fast pressurization events was used for the transient test simulations. Rapid test loop flow decreases, which are needed to simulate the very fast flow reductions in BWRs with internal pumps, was accomplished by rapid closure of a valve between the recirculation pump and the test section inlet.

Dynamic heater rod thermocouple responses are recorded as a function of time during the transient tests. In addition, transient test system response data are recorded in order to provide time-dependent boundary conditions for the transient system code simulations. The test section [

]^{a,c}

7.3.2 Test Section

The same SF24S, SF24SB, and SF24ST test sections used for the steady-state testing described in Section 3 were used for the transient tests.

7.3.3 Transient Tests Description

The D4.1.1 transient tests can be categorized as power increase or flow reduction transients for various axial power shapes, transient power and flow histories, and test section flow rates. All tests were performed for [

]^{a,c}

Each of the tests was performed with one of the axial power shapes shown in Tables 3.1 through 3.3. [

]^{a,c}

Power and flow transient events were simulated in the FRIGG Loop transient tests following two approaches. [

]^{a,c}

The [

]^{a,c}

The [

]^{a,c}

The power and flow transient profiles shown in Figures 7.1a through 7.2c, as well as [

]^{a,c}

The scope of the tests can be further clarified by grouping them according to axial power shape and categorization as power increase or flow reduction tests. Tables 7.1a and 7.1b, 7.2a and 7.2b, and 7.3a and 7.3b summarize the tests performed with the bottom-peaked, cosine-shape, and top-peaked axial power shapes, respectively. [

]^{a,c}

[

]^{a,c}

7.3.4 Dryout Threshold Temperature

The dryout threshold temperature is the temperature increase during the transient which is assumed to indicate dryout (e.g., Calculated CPR equals 1.0). The dryout threshold temperature in the transient tests was an increase of [

]^{a,c}

7.3.5 Transient Data

Sample test boundary conditions for a rapid power increase test (Test number 1391), a relatively slow power increase test (Test number 1446), and a flow reduction test (Test number 1414) are shown in Figures 7.3a, 7.4a, and 7.5a, respectively. The corresponding limiting rod temperature responses are shown in Figures 7.3b, 7.4b, and 7.5b, respectively. These tests were performed with a cosine axial power shape using Test Section SF24S. These figures show the test section power and coolant inlet flow as functions of time. The inlet coolant flow measurement is used as a boundary condition in the transient code simulations. [

]^{a,c}

For the [

]^{a,c}

The relatively [

]^{a,c}

Test number 1414 is an example of a [

]^{a,c}

It should be noted that the entire signal recording time range is not shown in Figures 7.3a through 7.5b. Only 10 seconds of the transients in Test Numbers 1391 and 1414 are shown, of which about 2 seconds is initial steady-state operation. Thirty seconds of the transient for Test Number 1446 is shown, of which about 2 seconds is initial steady-state operation.

The raw temperature signals leading to the type of traces in Figures 7.3b, 7.4b, and 7.5b [

]^{a,c}

The traces in Figures 7.3a through 7.5b are provided to illustrate the type of temperature responses for typical test power and flow histories used in the SVEA-96 Optima2 tests. Plots such as those shown in Figures 7.3a through 7.5b provide physical insight into the transient response to the test boundary conditions and assure that any anomalies are detected.

Tables 7.4 through 7.6 summarize the measured results from all of the transient tests.

7.4 IMPLEMENTATION VALIDATION FOR BISON CODE

The BISON-SLAVE channel model in the time domain reactor dynamics code BISON (References 4 and 5) will be used in conjunction with the D4.1.1 CPR correlation to predict transient CPR behavior for reload fuel licensing analysis applications. The BISON-SLAVE simulations presented in this section are an illustration of the methodology described in Section 7.2 for confirming that the use of a CPR correlation based on steady-state data is acceptable for transient application.

An overview of the BISON code and test section model is described below. The transient test simulation results are compared with the measurements.

7.4.1 BISON Code

BISON is a time domain BWR dynamics code used for analyzing operational and safety related transients. The code simulates the hydraulics of the entire primary core coolant loop including the recirculation pumps. A two-group diffusion theory model describes the axial distributions of neutron flux and power in the reactor core. Heat conduction in the fuel is solved in the radial direction at each axial segment. The influence from external systems such as the turbine, control systems, scram signals, and relief valves can also be simulated in BISON.

The BISON-SLAVE module of the code is used for the simulation of a single bundle in the core by utilizing boundary conditions from a BISON systems calculation for the entire reactor. It can also be used in a stand-alone mode to study heated bundles in loop experiments. External boundary conditions in the form of inlet mass flow and temperature, inlet pressure, and assembly power are supplied as input to the code. This option was used in the present evaluation to calculate the transient critical power ratio (CPR) for the experiments performed.

The D4.1.1 CPR correlation is incorporated in the BISON-SLAVE code. Instantaneous fluid properties (e.g., [ ]^{a,c}) are used in evaluating the CPR correlation under transient conditions.

7.4.2 BISON Model

The [ ]^{a,c} are modeled in the BISON simulations of the tests. The heated part of the test section is simulated with the BISON-SLAVE channel model. The heater rod is modeled with the same radial nodal divisions typically used in plant calculations. The radial representation and material compositions of the heater rod are shown in Figure 7.6.

The experimental conditions described in the previous sections were used as input to the BISON-SLAVE model. [

]^{a,c}

The R-factors derived from the local power distributions used in the power increase and flow reduction tests were determined using the R-factor models described in Section 5 [

]^{a,c}

7.4.3 BISON Test Simulation Results

All [ ]^{a,c} tests were simulated with the BISON-SLAVE code. The initial and boundary conditions input to each BISON-SLAVE test point simulation, the predicted and measured times to dryout, the experimental temperature change indicating whether or not dryout occurred, and the predicted minimum CPR for each test are listed in Tables 7.4 to 7.6 for the bottom-peaked, cosine-shaped, and top-peaked axial power distributions, respectively. Figures 7.7 through 7.9 show the [ ]^{a,c}. Table 7.7 provides clarification of Figures 7.7 through 7.9. As discussed in Section 7.3.4, dryout is indicated in the test results by the criterion of a maximum temperature change greater than or equal to [ ]^{a,c}. Dryout is indicated in the BISON-SLAVE simulation by a CPR prediction less than 1.0. A non-conservative BISON-SLAVE prediction occurs when the dryout is indicated by the test but not by the simulation (MCPR > 1.0). Therefore, a non-conservative BISON-SLAVE prediction is indicated [

]^{a,c}

As shown in Tables 7.4 through 7.6 and Figures 7.7 through 7.9, [

]^{a,c}

[

]^{a,c}

A further demonstration of the capability of the BISON-SLAVE/D4.1.1 to predict transient CPR response is the comparison of [

]^{a,c}

7.5 SUMMARY

The systematic Westinghouse methodology used to confirm the conservative application of a CPR correlation for transient CPR code applications is illustrated in this section for the D4.1.1 CPR correlation and BISON-SLAVE channel model. Comparisons of BISON-SLAVE code predictions with SVEA-96 Optima2 sub-bundle test results in this section demonstrate that the D4.1.1 CPR correlation is capable of providing conservative estimates of the onset of dryout during transients. It is concluded that the D4.1.1 correlation used in the BISON-SLAVE channel model provides sufficiently conservative predictions of the transient dryout test data to demonstrate that the D4.1.1/BISON-SLAVE combination will not underestimate the CPR response of the operational transients to which it will be applied and will support conservative CPR operating limits.

Table 7.1a SF24SB – Test Matrix for Power Increase Transients with Bottom-Peaked Axial Power Shape

a,c

Table 7.1b SF24SB – Test Matrix for Flow Decrease Transients with Bottom-Peaked Axial Power Shape

a,c

Table 7.2a SF24S – Test Matrix for Power Increase Transients with Cosine Axial Power Shape

a,c

Table 7.2b SF24S – Test Matrix for Flow Decrease Transients with Cosine Axial Power Shape

a,c

Table 7.3a SF24ST – Test Matrix for Power Increase Transients with Top-Peaked Axial Power Shape

a,c

Table 7.3b SF24ST – Test Matrix for Flow Decrease Transients with Top-Peaked Axial Power Shape

a,c

Table 7.4 SF24SB – Bottom-Peaked Test Results and BISON/SLAVE Predictions

a,c

Table 7.4 (cont.) SF24SB – Bottom-Peaked Test Results and BISON/SLAVE Predictions

a,c

Table 7.4 (cont.) SF24SB – Bottom-Peaked Test Results and BISON/SLAVE Predictions

a,c

Table 7.4 (cont.) SF24SB – Bottom-Peaked Test Results and BISON/SLAVE Predictions

a,c

Table 7.4 (cont.) SF24SB – Bottom-Peaked Test Results and BISON/SLAVE Predictions

a,c

Table 7.5 SF24S – Cosine Test Results and BISON/SLAVE Predictions

a,c

Table 7.5 (cont.) SF24S – Cosine Test Results and BISON/SLAVE Predictions

a,c

Table 7.5 (cont.) SF24S – Cosine Test Results and BISON/SLAVE Predictions

a,c

Table 7.5 (cont.) SF24S – Cosine Test Results and BISON/SLAVE Predictions

a,c

Table 7.5 (cont.) SF24S – Cosine Test Results and BISON/SLAVE Predictions

a,c

Table 7.6 SF24ST – Top-Peaked Test Results and BISON/SLAVE Predictions

a,c

Table 7.6 SF24ST – Top-Peaked Test Results and BISON/SLAVE Predictions (cont.)

a,c

Table 7.7 Criteria for Non-Conservative Prediction of Transient CPR Prediction

a,c

a,c

Figure 7.1a Power Profiles

a,c

Figure 7.1b Power Profiles Used for Power Transients

a,c

Figure 7.1c Power Profiles Used for Power Transients

a,c

Figure 7.1d Power Profiles Used for Power Transients

a,c

Figure 7.2a Flow Profiles Used for Flow Reduction Transients

a,c

Figure 7.2b Flow Profiles

a,c

Figure 7.2c Flow Profiles

a,c

Figure 7.3a Power Increase Transient – Power and Mass Flux as Function of Time Experiment Number 1391

a,c

Figure 7.3b Power Increase Transient – Measured Temperature – Experiment Number 1391

a,c

Figure 7.4a Power Increase Transient (Slow) – Power and Mass Flux as Function of Time Experiment number 1446

a,c

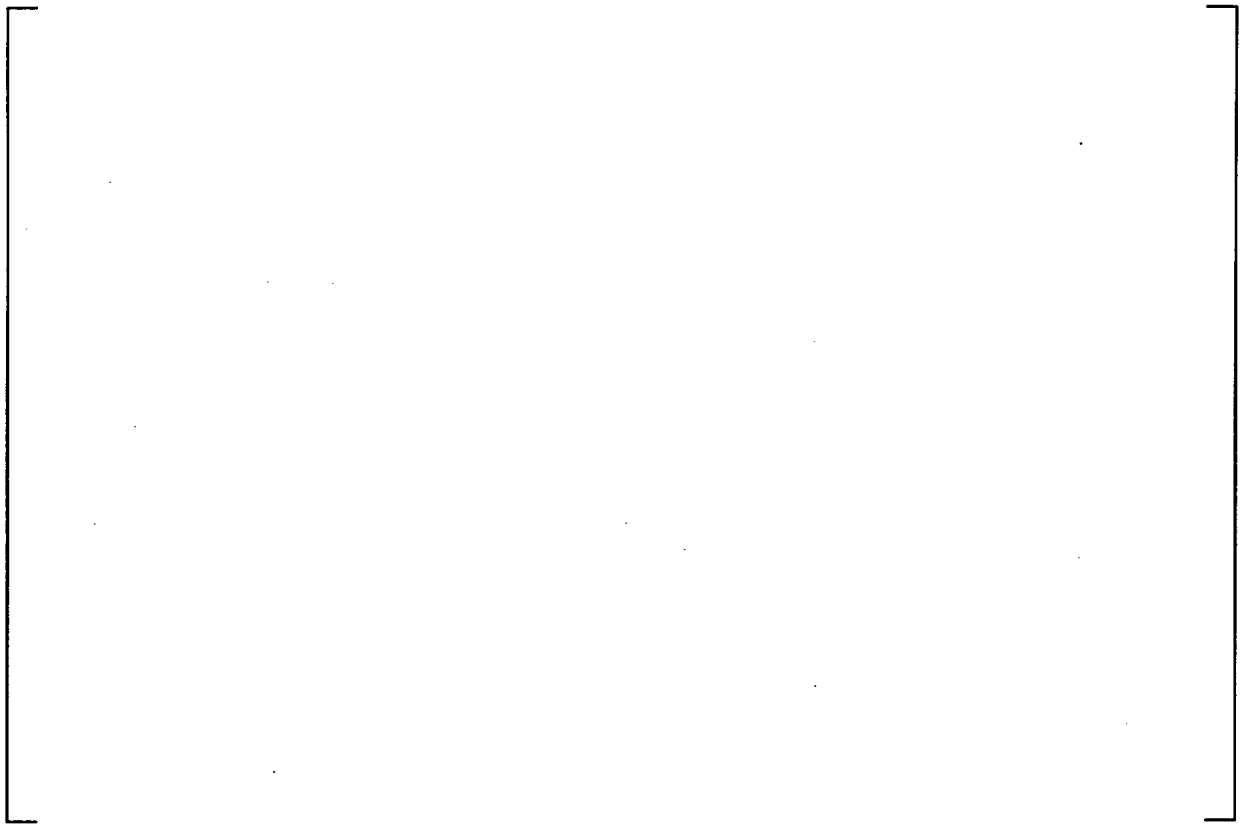

Figure 7.4b Power Increase Transient (Slow) – Measured Temperature – Experiment Number 1446

a,c

Figure 7.5a Flow Reduction Transient – Power and Mass Flux as Function of Time Experiment Number 1414

a,c

Figure 7.5b Flow Reduction Transient – Measured Temperature – Experiment Number 1414

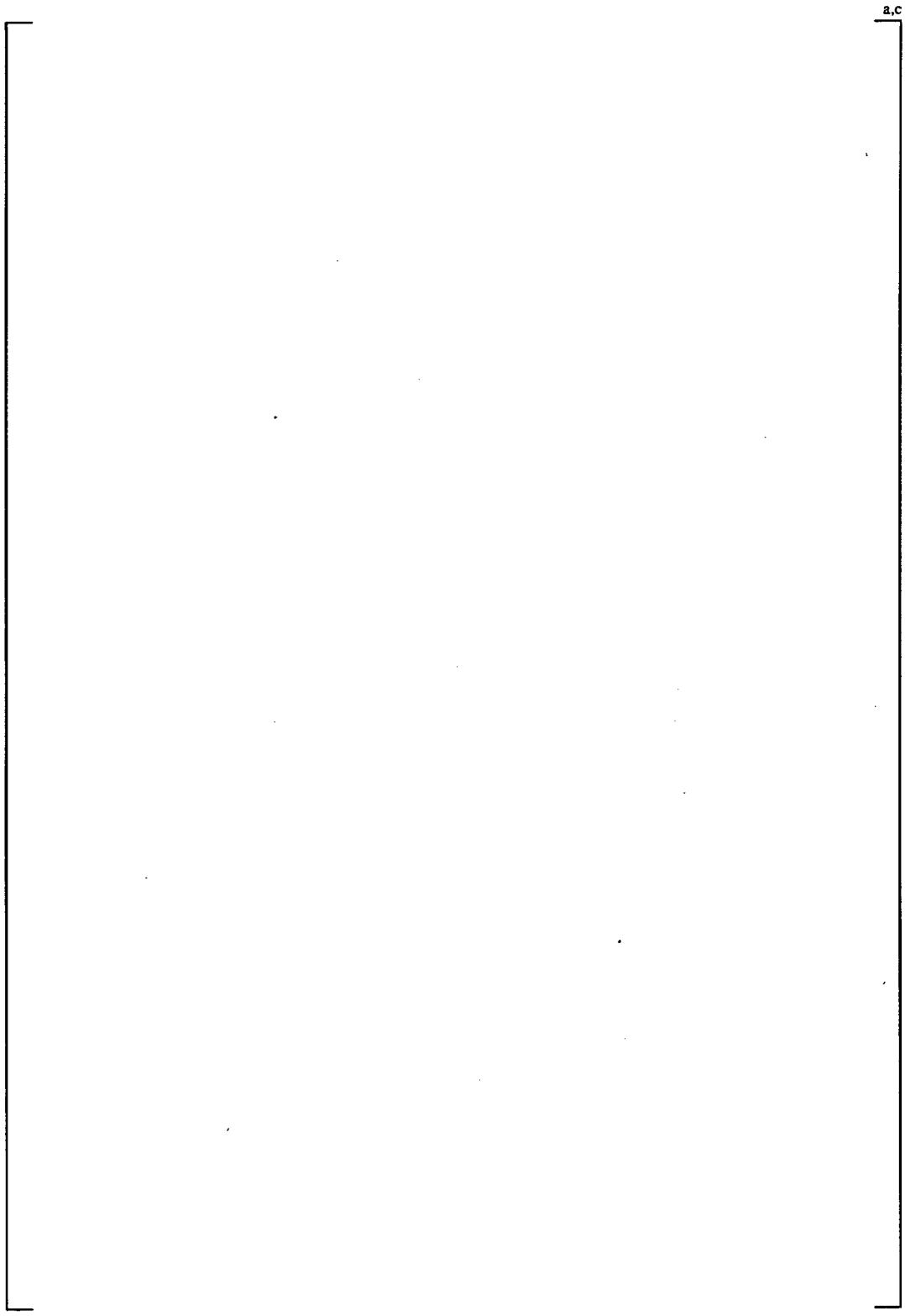

Figure 7.6 BISON-SLAVE Model for Test Heater Rod

a,c

Figure 7.7 Transient Validation for SF24SB – Bottom-Peaked Axial Power Shape

a,c

Figure 7.8 Transient validation for SF24S – Cosine Axial Power Shape

a,c

Figure 7.9 Transient Validation for SF24ST – Top-Peaked Axial Power Shape

a,c

Figure 7.10 Measured Time to Boiling Transition vs. Predicted Time

8 CONCLUSIONS

The critical power measurements described in this report provide an accurate simulation of the SVEA-96 Optima2 fuel assembly. A total of [ ]^{a,c} 24-rod sub-bundle data points covering the entire range expected during reactor operation were obtained. The D4.1.1 critical power ratio correlation was developed to correlate this critical power data. The correlation was developed to provide best estimate predictions of critical power for a SVEA-96 Optima2 fuel assembly. The mean prediction error and standard deviation over the entire range of validity are [ ]^{a,c}.

Based on the critical power data for SVEA-96 Optima2 and the evaluations of the data presented in this report, the following conclusions can be drawn:

1. Sufficient data have been obtained to justify the use of the correlation over the following ranges for design and licensing applications in following table:

a,c

These ranges cover the operating conditions expected during U.S. BWR steady-state, transient, or accident conditions over which CPR calculations are expected to be required.

2. The correlation provides a best estimate of the bundle Critical Power Ratio over the range of validity and, is, therefore, acceptable for evaluations of Critical Power Ratios for design and licensing purposes over this range.

3. The mean prediction error and standard deviation to be utilized for the correlation for design and licensing applications is [ ]^{a,c}, respectively, over the entire range of validity of the correlation. Specifically, a mean error of [ ]^{a,c} are appropriate to support the Safety Limit Minimum Critical Power Ratio (SLMCPR) computations.

4. The correlation has been demonstrated to be capable of providing conservative estimates of the onset of dryout during fast transients. The capability of the correlation to provide conservative estimates of the onset of dryout during fast transients is demonstrated for each transient system

code application. An illustration of the Westinghouse methodology for confirming the capability of the correlation to conservatively treat transient applications is provided for the BISON-SLAVE code documented in References 4 and 5. It is demonstrated in this illustration that the correlation, in conjunction with the BISON-SLAVE code, is acceptable for the calculation of changes in CPR during transient events for design and licensing applications.

9 REFERENCES

1. "10x10 SVEA Fuel Critical Power Experiments and CPR Correlations: SVEA-96," Westinghouse Report CENPD-392-P-A, September, 2000.

2. "10x10 SVEA Fuel Critical Power Experiments and CPR Correlations: SVEA-96+," ABB Report CENPD-389-P, June 1998.

3. "Improved Application of Westinghouse Boiling length CPR Correlations for BWR Fuel," WCAP-16047-P, February 2002.

4. "BISON – A One Dimensional Dynamic Analysis Code for Boiling Water Reactors," ABB Report RPA 90-90-P-A, December 1991.

5. "BISON – One Dimensional Dynamic Analysis Code for Boiling Water Reactors: Supplement 1 to Code Description and Qualification," ABB Report CENPD-292-P-A, July 1996.

6. "General Electric BWR Thermal Analysis Basis (GETAB): Data, Correlation and Design Application," NEDO-10958, November 1973.

7. Second Japanese-European Two-Phase Flow Group Meeting "Loop Studies Simulating – in Annular Geometry – The Influence of The Axial Power Distribution and The number of spacers on Dryout in 8x8 BWR Assemblies," Jan Blomstrand et al., University of Tsukuba, Japan, 25-29 September 2000.

8. "CONDOR: A Thermal-Hydraulic Performance Code for Boiling Water Reactors," ABB Report BR 91-255-P-A, Rev. 1, (Proprietary), BR 91-262-NP-A (Non-proprietary), May 1991.

9. "The Advanced PHOENIX and POLCA Codes for Nuclear Design of Boiling Water Reactors," CENPD-390-P-A, Rev. 00, December 2000.